

# B-FROST: B-Fields and staR fOrmation across Scales with TRAO

## III: The high-energy $\lambda$ Orionis ring

E. Mannfors<sup>1</sup>, J. Montillaud<sup>2</sup>, J. Vorster<sup>1</sup>, J. Oers<sup>3</sup>, D. Alina<sup>4</sup>, M. Juvela<sup>1</sup>, C. W. Lee<sup>5,6</sup>, S. Li<sup>7,8</sup>, V.-M. Pelkonen<sup>9</sup>, I. Ristorcelli<sup>3</sup>, and L. V. Tóth<sup>10,11</sup>

<sup>1</sup> Department of Physics, P.O. box 64, FI- 00014, University of Helsinki, Finland  
e-mail: emma.mannfors@gmail.com

<sup>2</sup> Université Marie et Louis Pasteur, CNRS, Institut UTINAM (UMR 6213), OSU THETA, F-25000 Besançon, France

<sup>3</sup> IRAP, Université de Toulouse, CNRS, 9 Avenue du Colonel Roche, BP 44346, 31400 Toulouse Cedex 4, France

<sup>4</sup> Physics Department, School of Sciences and Humanities, Nazarbayev University, Kabanbay batyr ave, 53, Astana 010000 Kazakhstan

<sup>5</sup> Korea Astronomy and Space Science Institute, 776 Daedeokdae-ro, Yuseong-gu, Daejeon 34055, Republic of Korea

<sup>6</sup> University of Science and Technology, Korea (UST), 217 Gajeong-ro, Yuseong-gu, Daejeon 34113, Republic of Korea

<sup>7</sup> School of Astronomy and Space Science, Nanjing University, 163 Xianlin Avenue, Nanjing 210023, China

<sup>8</sup> Key Laboratory of Modern Astronomy and Astrophysics (Nanjing University), Ministry of Education, Nanjing University, Nanjing 210023, China

<sup>9</sup> INAF - Istituto di Astrofisica e Planetologia Spaziali, Via Fosso del Cavaliere 100, I-00133 Roma, Italy

<sup>10</sup> Eötvös Loránd University, Institute of Physics and Astronomy Budapest, Hungary

<sup>11</sup> University of Debrecen, Institut of Physics Debrecen, Hungary

Received Month Day, 1996; accepted Mo dd, 1997

## ABSTRACT

**Context.** High-mass stars affect their environment in complex ways but these feedback-dominated regions are still poorly understood. Due to their large distances, the study of high-mass stars is difficult. The  $\lambda$  Orionis region is a molecular ring surrounding the bright OB double star  $\lambda$  Orionis (Meissa) at a distance of only  $\sim 400$  pc.

**Aims.** We aim to understand the morphology and kinematics of this region using a combination of CO and continuum observations.

**Methods.** We have performed  $^{12}\text{CO}$  and  $^{13}\text{CO}$  ( $J=1-0$ ) observations of three dense regions in this ring with the TRAO 14-m telescope as part of the B-FROST survey. We estimate column densities, CO X-factors, and [CO/H<sub>2</sub>] abundances in these clouds. The clouds are subdivided into regions in PPV-space using dendograms. We compare these regions in the context of local environment: density, proximity to Meissa, morphological complexity, and molecular content. We use ancillary protostar and clump catalogs to understand star-formation properties of these clouds. We compare filament and magnetic (B-) field alignment using histograms of relative orientations.

**Results.** The strong UV radiation from Meissa is compressing and dissociating the cloud. In the Meissa-facing regions of the cloud, the transition from atomic to molecular H<sub>2</sub> and CO are cospatial at the TRAO resolution (48''). Dense filamentary structures, containing CO-cores, are located at the head of these regions. We detect depletion of  $^{13}\text{CO}$  as well as  $^{12}\text{CO}$  in several dense cores and the filamentary ridge in  $\lambda$  Orionis E (Barnard 35). In general, these structures do not seem to be gravitationally bound but it is likely some dense cores are pressure-confined. Mean [CO/H<sub>2</sub>] abundances are lower in  $\lambda$  Orionis compared to the canonical value of  $10^{-4}$ . This may be caused by uncertainties in column density estimates but also by the strong UV environment. B-fields and filaments are not strongly aligned, but are slightly more perpendicular at low  $^{12}\text{CO}$  intensity.

**Conclusions.**  $\lambda$  Orionis is a region clearly affected by stellar feedback. Low gravitational boundedness suggests a region being dispersed by UV radiation, with the exception of some dense cores and filamentary structures. Stellar feedback is likely to dominate over magnetic energy in this region. These findings will enable comparison with other B-FROST targets in future papers.

**Key words.** ISM: clouds – Methods: observational – ISM: individual objects:  $\lambda$  Orionis, BRC-18, Barnard 35, Barnard 30, Barnard 223 – ISM: lines and bands – ISM: abundances Infrared: ISM

## 1. Introduction

Most of the dense interstellar medium (ISM) is cold, shielded from the interstellar UV radiation field by outer layers of atomic gas. However, near bright OB stars UV radiation and stellar winds shape the ISM in complex ways. While comparatively rare, high-mass stars are crucial for the evolution of galaxies. OB stars ionize their environment, carving out ionized H II regions and disrupting star formation (SF). However, high-mass

stars can also compress gas and trigger further generations of SF. Due to the rarity and large distances, the effect of OB stars on the ISM is not yet well understood. The  $\lambda$  Orionis ring lies at the outer edges of an H II region carved out by the bright OB star  $\lambda$  Orionis (hereafter Meissa). As a nearby field at a distance of around 400 pc,  $\lambda$  Orionis is an ideal region with which to study stellar feedback.

Dense molecular clouds (MCs) are primarily composed of molecular hydrogen (Ferrière 2001). As H<sub>2</sub> is a symmetric

molecule with no dipole moment, it does not emit at the low temperatures in the dense ISM (Heyer & Dame 2015). Instead, in the majority of cases astronomers must estimate H<sub>2</sub> column densities using more easily observed molecules. Carbon monoxide (CO) is one of the most common molecules in the ISM and emits at millimeter wavelengths at the temperature of the dense ISM (Bolatto et al. 2013; Heyer & Dame 2015).

The formation and destruction pathways of H<sub>2</sub> and CO are different, and thus comparing the two can give a deeper understanding of the physics within dense MCs. Formation of H<sub>2</sub> is slow, occurring on dust grains. It is dissociated by UV radiation (Gould & Salpeter 1963; Hollenbach & Salpeter 1971; Heyer & Dame 2015). Although CO is also sensitive to UV radiation, it forms in the gas phase and is thus not dependent on dust abundances for formation (Heyer & Dame 2015). While the boundary is dependent on the metallicity and local radiation field, hydrogen is generally molecular at column densities above 10<sup>20</sup> cm<sup>-2</sup> (Hollenbach et al. 1971; McKee & Krumholz 2010; Sternberg et al. 2014). Modeling of photodissociation regions suggests carbon is bound into molecules only at column densities exceeding 10<sup>21</sup> cm<sup>-2</sup> (Visser et al. 2009). When densities increase sufficiently, CO freezes out onto dust grains leading to depletion of the molecule in the gas phase (Bergin et al. 1995; Acharyya et al. 2007). This process is less efficient for more massive molecules, thus <sup>12</sup>CO freeze-out usually occurs at lower densities than <sup>13</sup>CO freeze-out. Due to these effects, CO is believed to be good tracer for H<sub>2</sub> only at extinction  $A_v \approx 2 - 7$  mag (Pineda et al. 2008; Ripple et al. 2013; Heyer & Dame 2015), which can be related to hydrogen column density  $N(H_2)$  with  $N(H_2)/A_v = 10^{21} \text{ cm}^{-2} \text{ mag}^{-1}$  (Bohlin et al. 1978; Sadavoy et al. 2012).

A CO-to-H<sub>2</sub> abundance ratio [CO/H<sub>2</sub>] of  $\sim 10^{-4}$  has been estimated for the Galaxy (Herbst & van Dishoeck 2009) and similar values have been observed for nearby MCs such as Taurus and Orion B (Pineda et al. 2010; Roueff et al. 2021). However, even within a single region the abundance can change by a factor of a few (Roueff et al. 2021). Abundance is affected by local conditions (temperature, radiation fields) and gas and dust composition (including metallicity), and thus the study of CO abundances can be used to understand the morphology and environment of MCs.

$\lambda$  Orionis is a ring of cold gas of diameter  $\sim 10^\circ$  (Maddalena & Morris 1987) surrounding the bright multiple star Meissa in the head of the Orion constellation (Fig. 1). Using kinematic modeling Maddalena & Morris (1987) estimate that this ring is expanding at a rate of 14 km s<sup>-1</sup> and is tilted by 36° with respect to the line of sight with the southwest section of the ring being closest to the Sun. Lang et al. (2000) estimate a total molecular mass of  $1.4 \times 10^4 M_\odot$  for the  $\lambda$  Orionis ring. Zucker et al. (2019) use Gaia parallaxes to estimate a distance of  $402 \pm 20$  pc to  $\lambda$  Orionis. The Meissa system is composed of two stars of spectral classes O8III and B0Ve at a distance of  $417 \pm 10$  pc (de Almeida et al. 2019). The primary component has a K-band magnitude of 3.876 mag, effective temperature of  $35.0_{-1.5}^{+2.0} \times 10^3$  K, and a mass of  $\sim 26.1_{-9.5}^{+15.1} M_\odot$  (Cutri et al. 2003; de Almeida et al. 2019). It is surrounded by the H II region Sh2-264 which has a radius of  $\sim 4^\circ$  (Maddalena & Morris (1987); Fig. 1).

$\lambda$  Orionis shows clear signs of energetic feedback. Chuss et al. (2022) observed significant PAH features at  $3.3 \mu\text{m}$  with the DIRBE instrument on the COBE satellite. These features are especially strong at the location of the three regions studied in this paper, reaching  $0.4 \text{ MJy sr}^{-1}$  according to their Fig. 3. Comparison of the  $\lambda$  Orionis region with the nearby Orion A and B clouds (also labeled on Fig. 1), shows significantly lower de-

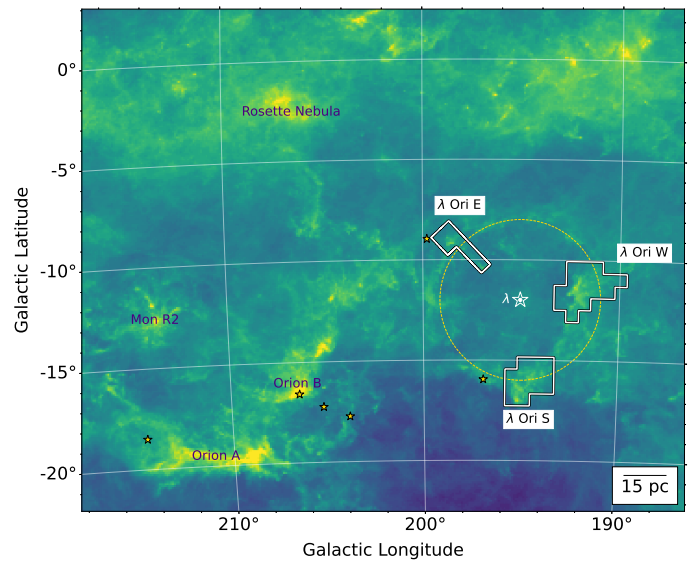


**Fig. 1.** The three observed regions (white outlines) shown on a Planck 857 GHz map. Meissa is marked with a white star, and the approximate extent of the H II region ( $\sim 4^\circ$ ) is drawn with a yellow dashed circle. The Galactic plane is at the top of the image. Various well-known MCs are also labeled. The familiar stars of the Orion constellation are drawn with black stars. The scalebar in the lower right corresponds to a distance to Orion of 402 pc.

tection rates of dense gas tracers (N<sub>2</sub>H<sup>+</sup>, HCO<sup>+</sup>, and H<sup>13</sup>CO<sup>+</sup>) and a relatively high ratio of  $N(\text{N}_2\text{H}^+)/N(\text{HCO}^+)$ . The authors suggest that photoevaporation caused by Meissa has destroyed dense gas in  $\lambda$  Orionis which is still present in Orion A and B, and has further significantly delayed core evolution. Using polarization observations and Gaia proper motions of young stellar objects (YSOs) connected with the Meissa-facing head of the  $\lambda$  Orionis E field, Saha et al. (2022) have found that the YSOs are moving away from Meissa. The vector of their proper motion seems to be nearly parallel to the direction of the ionizing radiation, suggesting that UV wind from Meissa is dispersing the cloud and natal YSOs. A lower number of Planck Galactic Cold Clumps (PGCCs) can be found in  $\lambda$  Orionis compared to Orion A and B (Yi et al. 2018). According to the PGCC, the cores in  $\lambda$  Orionis have higher dust temperatures ( $T_d \approx 16$  K) and lower dust emissivity spectral index ( $\beta \approx 1.65$ ), compared to  $T_d \approx 13 - 14$  K and  $\beta \approx 1.9 - 2.0$  in Orion A and B. The cores in  $\lambda$  Orionis also have much smaller size, column and number density, and consequently mass ( $R \sim 0.08$  pc,  $N(\text{H}_2) \sim 9.5 \times 10^{22} \text{ cm}^{-2}$ ,  $n(\text{H}_2) \sim 3 \times 10^5 \text{ cm}^{-3}$ ,  $M \sim 1 M_\odot$ ), whereas column densities in Orion A and B reach  $10^{23} \text{ cm}^{-2}$  and masses over  $2 M_\odot$ .

$\lambda$  Orionis East (hereafter E) is also known as the Barnard 35 dark cloud (Barnard 1919, 1927) and Bright-Rimmed Cloud-(BRC-) 18 (Sugitani et al. 1991). The center of E is located  $\sim 31$  pc from Meissa assuming distances of 417 pc and 402 pc to Meissa and  $\lambda$  Orionis E, respectively. This region consists of two main structures connected (in the plane of the sky) by a more diffuse bridge. Using 850  $\mu\text{m}$  SCUBA-2 continuum observations, Yi et al. (2018) detected four clumps and four dense cores, two of which they classify as protostellar (Fig. 2).  $\lambda$  Orionis West (hereafter W) is also known as the Barnard 30 dark cloud and BRC-17. The center of this region is located  $\sim 41$  pc from Meissa. W consists of one main structure, with streamers extending behind the cloud, away from Meissa. Yi et al. (2018) detected 10 clumps and 7 dense cores, one of which is protostellar (PGCC 192.1-10.9A1 S).  $\lambda$  Orionis South (hereafter S) is

also known as the Barnard 223 dark cloud, located at a distance of  $\sim 46$  pc from Meissa. It consists of a more dense region in the south, with more diffuse structures extending to the northeast (toward Meissa). Yi et al. (2018) detected ten clumps in S.

By combining continuum and molecular line observations, we seek to understand the structure and environment of the  $\lambda$  Orionis ring including molecular abundances and the CO X-factor. We present a thorough study of a high-energy irradiated ring at core-scale resolution, which can in the future be compared to the other sources in the B-FROST survey. This paper is structured as follows: We present our TRAO observations and ancillary data acquisition in Sect. 2. Calculations of dust properties, CO X-factors, abundances, and structural analysis are described in Sect. 3. We present results in Sect. 4 which we discuss in Sect. 5.

## 2. Observations and data reduction

### 2.1. Observations

B-FROST, a key science program (KSP) on the Taeduk Radio Astronomy Observatory (TRAO; Jeong et al. (2019)), mapped MCs in six Galactic fields. The B-FROST sources cover clouds in a wide range of environments, from low-mass, isolated SF regions to regions affected by feedback from massive stars (e.g.  $\lambda$  Orionis). The B-FROST survey is introduced in Montillaud et al., *in prep* (hereafter BFROST-I).

TRAO is a 13.7 m telescope located in Taeduk, Deajeon, Yuseong-gu, South Korea, and is operated by the Korea Astronomy and Space Science Institute (KASI)<sup>1</sup>. B-FROST observations were performed with TRAO in November–December 2021, January–March and Nov–Dec 2022, and Jan–Mar 2023.  $\lambda$  Orionis was observed toward the end of this period. Observing conditions for the three fields are listed in Table 1. In  $^{13}\text{CO}$  observations, over 90% of all pixels have random mean squared (RMS) error below the target value of 0.15 K. The percentage is slightly lower for  $^{12}\text{CO}$ , but these poor-quality pixels were generally at the map edges and have been masked out. The observations and reduction of these data are presented in more detail in BFROST-I. Due to issues in baseline,  $^{13}\text{CO}$  observations of  $\lambda$  Orionis W are not used (see Appendix A). Thus we do not calculate CO column densities or other properties derived using  $^{13}\text{CO}$  for this field. The resolution of the TRAO telescope is  $48''$ , corresponding to a physical resolution of  $\sim 0.1$  pc at 400 pc. TRAO spectral line observations have been smoothed to a velocity resolution of  $0.2 \text{ km s}^{-1}$ .

### 2.2. Ancillary data

We use archival ancillary data from multiple telescopes to further our analysis. The European Space Agency (ESA) *Planck* satellite has observed the whole sky in both continuum and polarization at a resolution of  $5'$ . We use column density  $N(\text{H}_2)$  derived from *Planck* 353 GHz optical depths as well as *Planck* polarization maps. Further, the two dense regions in  $\lambda$  Orionis E have been mapped with the *Herschel* space telescope at a resolution of  $\sim 40''$  or better (Fig. 3)<sup>2</sup>. We name these the Front and Rim regions to correspond with the dendrogram regions (see Sect. 3.1; Observation IDs 1342227710 and 1342216932, respectively). Extinction data at a resolution of  $2'$  are extracted

from the iNICEST platform<sup>3</sup> (Lombardi & Alves 2001; Lombardi 2009). We collected HI data (column density and spectra) from the HI4PI survey (HI4PI Collaboration et al. 2016). From the HI4PI data we have extracted two cubes, (SIN E10 at  $\ell=190^\circ$ ,  $b=0^\circ$ ; SIN D10 at  $\ell=190^\circ$ ,  $b=-20^\circ$ ). HI column densities were extracted from the HEALPIX data<sup>4</sup>.

## 3. Methodology

### 3.1. Computation of dendograms and designation of subregions

To understand the multiscale nature of these regions, we use AstroDendro (Rosolowsky et al. 2008; Robitaille et al. 2019) to divide the CO datacubes into dendograms. This program decomposes astronomical data into interconnected regions and can describe the structure of clouds at different scales. The minimum emission for a pixel to be included in a dendrogram was set to  $\sim 4\sigma$  of the full datacube. Structures are required to be a minimum of 54 pixels (around 10 times the area of the beam in pixels) in size to reduce the prevalence of noise peaks. We describe the dendrogram inputs in Appendix B. Based on the dendograms we have divided our data into subregions, shown in Fig. 4. Unlike the more simple regions in BFROST-I, these subregions are based on the PPV structure of the clouds. E is divided into three regions: the Rim, Center, and Front. S is divided into three (two) regions in  $^{12}\text{CO}$  ( $^{13}\text{CO}$ ), with the High-Velocity Cloud not being detected in  $^{13}\text{CO}$ . W is the most complex, being divided into the Body, Wings, Spine, and Back and Front Legs.

### 3.2. Filament detection and comparison with magnetic fields

#### 3.2.1. Magnetic fields

We have extracted B-field maps from *Planck* polarization data ( $FWHM \sim 5'$ ). The Stokes  $I$ ,  $Q$ , and  $U$  vectors can be used to calculate polarization angle  $\Psi_B$  and polarization fraction  $p$  (Planck Collaboration et al. 2015)

$$\Psi_B = 0.5\text{atan}(U, Q) + \pi/2, \quad (1)$$

$$p = \frac{\sqrt{Q^2 + U^2}}{I}. \quad (2)$$

$\Psi_B$  ranges from  $[-90^\circ, 90^\circ]$  but increases clockwise from Galactic north in convention with the HEALPIX software. To calculate polarization angle corresponding to IAU conventions,  $\Psi_B$  can be calculated as  $\Psi_{B;\text{IAU}} = 0.5\text{atan}(-U, Q) + \pi/2$  (Planck Collaboration et al. 2015).

#### 3.2.2. FilDReaMS

We have applied the FilDReaMS (Filament Detection and Reconstruction at Multiple Scales; Carrière et al. 2022b) algorithm to the  $W(^{12}\text{CO})$  maps of the three fields. FilDReaMS detects filaments at multiple scales in astronomical data, returning their widths and orientations. The algorithm fits a rectangular model bar with width  $W_b$ , length  $L_b$ , and aspect ratio  $r_b = L_b/W_b$  to detect elongated structures. The orientation angle  $\Psi_b$  of the model bar is given with respect to Galactic north and increases counterclockwise from North consistent with IAU conventions

<sup>3</sup> <http://interstellarclouds.fisica.unimi.it/html/index.html>

<sup>4</sup> [https://vizier.cds.unistra.fr/viz-bin/VizieR-3?-source=J/A%2bA/594/A116/nhi\\_hpx](https://vizier.cds.unistra.fr/viz-bin/VizieR-3?-source=J/A%2bA/594/A116/nhi_hpx)

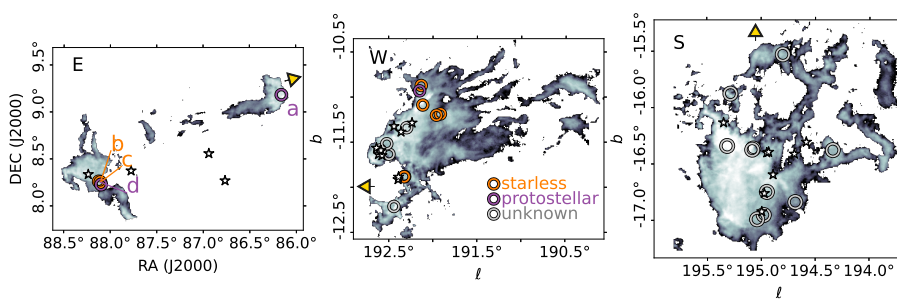


**Fig. 2.** Signs of star formation in the  $\lambda$  Orionis ring. YSOs from the Marton et al. (2019) YSO catalog that have Gaia parallaxes corresponding to  $402 \pm 5$  pc (marked with white stars). Planck Cold Clumps (PGCCs) from the Yi et al. (2018) catalog are marked with circles, with color corresponding to clump type: starless (orange), protostellar (purple), or unknown (light gray). The four cores in E are labeled and correspond to the PGCC clumps a) G196.92-10.37; b) G198.69-09.12 N1; c) G198.69-09.12 N2; d) G198.69-09.12 S.

**Table 1.** TRAO observations of the  $\lambda$  Orionis fields

(a) Field	(b) $\ell$ ( $^{\circ}$ )	(c) $b$ ( $^{\circ}$ )	(d) Map size ( $^{\circ}$ )	(e) $n_{\text{tiles}}$	(f) $t_{\text{obs}}$ (h)	(g) $\langle T_{\text{sys}} \rangle$ ( $^{12}\text{CO}$ K)	(h) $\langle T_{\text{sys}} \rangle$ ( $^{13}\text{CO}$ K)	(i) $\langle \text{wvp} \rangle$ (mm)	(j) Pixels in target ( $^{12}\text{CO}$ %)	(k) Pixels in target ( $^{13}\text{CO}$ %)
East	198.119	-9.508	3.33×3.33	7	99	$724 \pm 245$	$340 \pm 146$	$5.3 \pm 2.5$	64	95
West	191.765	-11.507	3.71×3.07	17	226	$610 \pm 151$	$272 \pm 69$	$4.3 \pm 2.1$	73	96
South	194.544	-16.055	2.78×2.78	13	186	$664 \pm 136$	$294 \pm 70$	$4.8 \pm 2.7$	76	99

**Notes.** Columns (b-h) reproduced from BFROST-I. The columns are: (a) Name of the cloud; (b-c) galactic coordinates of the center of the image; (d) map angular size; (e) number of tiles; (f) total TRAO observing time per target (pointing and focus not included); (g, h) average system temperature at 115 GHz and 110 GHz, respectively; (i) mean water vapor pressure; (j,k) percent of pixels within the target RMS in  $^{12}\text{CO}$  and  $^{13}\text{CO}$ , respectively.

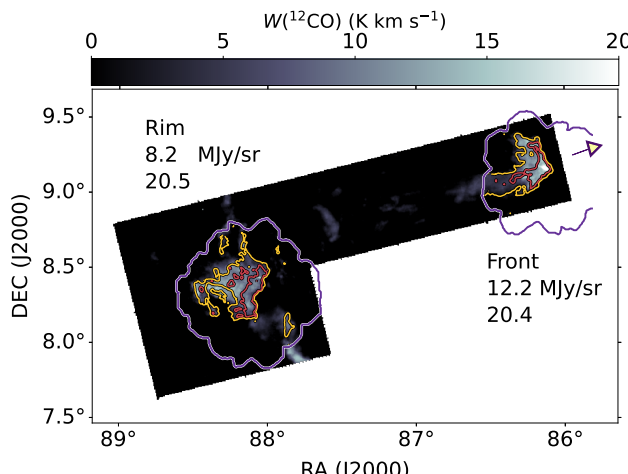


**Fig. 3.**  $^{12}\text{CO}$  moment map of  $\lambda$  Orionis E. The contours show the outlines (purple contours) and the 80 and 99<sup>th</sup> intensity percentiles of the *Herschel* 500  $\mu\text{m}$  maps (yellow and red, respectively). The intensity at each contour is printed on the plot. The arrow points toward Meissa.

(Hamaker & Bregman 1996). As the model bar is symmetric this angle is given in the range  $[-90^{\circ}, 90^{\circ}]$ .

FilDReaMS is a multiscale algorithm, as for each filament width  $W_b$  it filters out structures larger than  $W_b$ . For each pixel  $i$  of this filtered map the code fits a model bar centered on  $i$ , deriving the best-fit orientation angle  $P_{b,i}$  and calculates a significance  $S_i$  of the detection based on comparisons with an ideal filament. For matches with  $S_i > 1$  the structure is marked as a filament with filament orientation angle  $\Psi_{f,i} = \Psi_{b,i}$ . Its shape is extracted from the filtered map and its intensity from the original map. Finally, FilDReaMS superimposes all detected filaments at each pixel, assigning to each filament the orientation angle of the most significant fit within the network. This process is repeated for different widths until a network of filaments at multiple scales is detected.

To qualify as a potential filament, we require  $r_b \geq 3$  as in Carrrière et al. (2022a) and accept filament widths  $W_b$  in the range  $[W_{b,\min}, W_{b,\max}]$  where  $W_{b,\min} = 5$  pix (0.22 pc) and  $W_{b,\max}$  is the largest structure detected in the field. Due to boundary limitations during the filtering process, structures larger than  $W_{b,\max}$  may remain undetected. Maximum  $W_b$  in the three fields are 7 pix, 12 pix, and 13 pix (0.3 pc, 0.52 pc, and 0.56 pc) for E, W, and S, respectively.

Whether filaments are parallel or perpendicular to the magnetic (B-) field has been found to depend on column density (Planck Collaboration et al. 2016), but this relative orientation has been observed to vary within the ISM (Pattle et al. 2023). The relative orientation between filaments and the B-field can be analyzed with the Histogram of Relative Orientations (HRO; Soler et al. 2013), which we use to describe the relative orientation  $\Delta\Psi$  as a function of intensity (or column density,  $W(\text{CO})$ , or another analogous quantity) at multiple scales. We calculate the relative angle between the filament  $\Psi_f$  and the B-field position angle  $\Psi_B$

$$\Delta\Psi = |\Psi_f - \Psi_B|. \quad (3)$$

### 3.3. Dust analysis and estimation of $H_2$ column density

The spectral energy distribution (SED) of a MC can be fitted with a modified blackbody (MBB) formula.

$$I_\nu = I_{\nu,0} \frac{B_\nu}{B_{\nu,0}} \left( \frac{\nu}{\nu_0} \right)^\beta, \quad (4)$$

where  $I$  is the intensity at frequency  $\nu$  and reference frequency  $\nu_0$ ,  $B_\nu$  is the Blackbody function, and  $\beta$  is the value of the dust opacity spectral index. Dust temperature and  $\beta$ , derived from Eq. 4 can be used to estimate Hydrogen column density  $N(H_2)$ .

$$N(H_2) = N_H = \frac{I_\nu}{B_\nu(T)\kappa_\nu m_H}, \quad (5)$$

where dust opacity  $\kappa_\nu$  can be expressed as  $\kappa_\nu = \kappa_0(\nu/\nu_0)^\beta$ ,  $\mu = 2.8$  is the mean molecular weight per free particle, and  $m_H$  is the

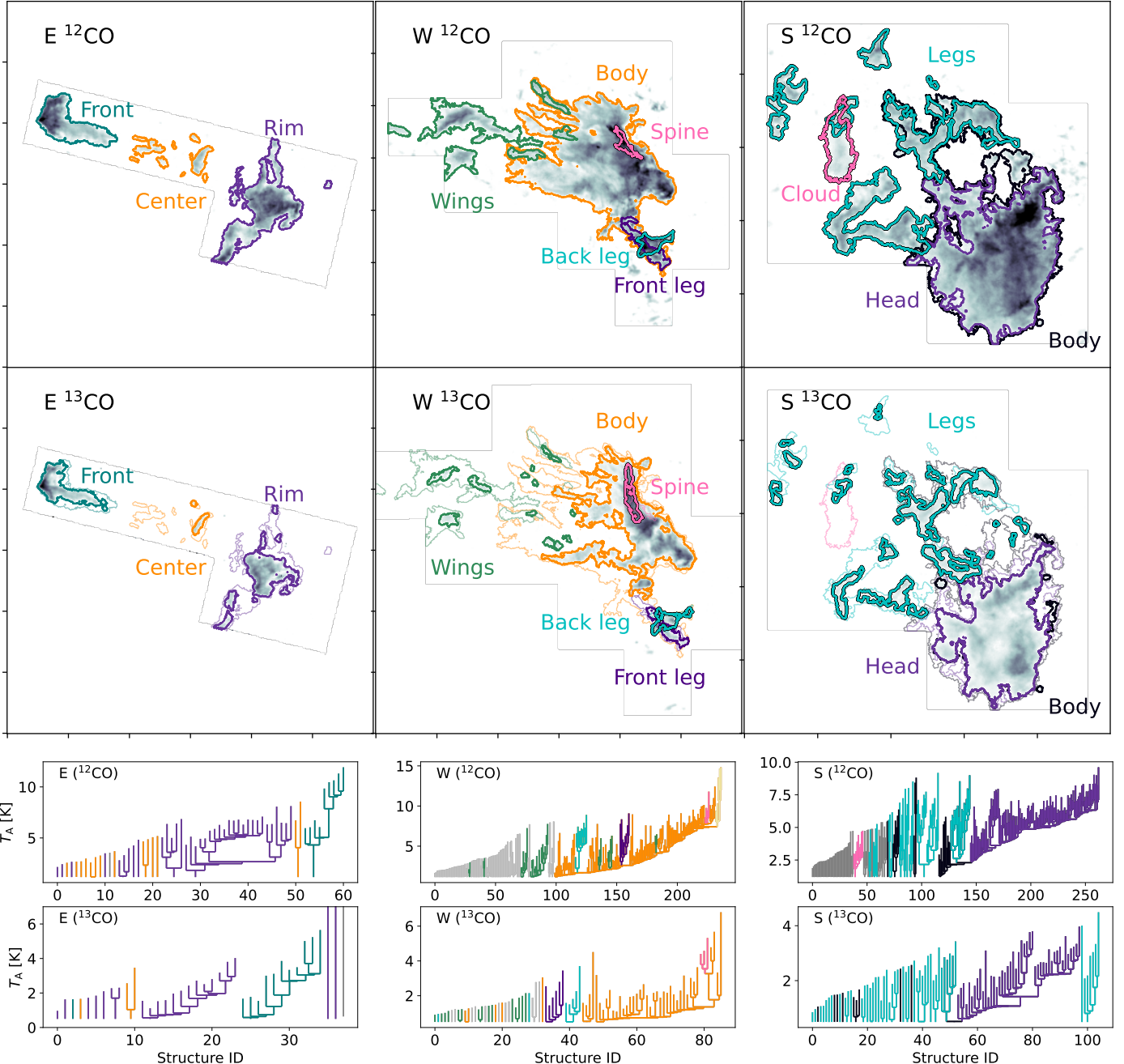


**Fig. 4.** Regions extracted from the dendrograms. (Top): Regions in the  $^{12}\text{CO}$  map. (Center): Regions in the  $^{13}\text{CO}$  map. The fainter lines show the extent of the  $^{12}\text{CO}$  regions. (Bottom two rows): Tree plots of the dendrogram structure. (Left):  $\lambda$  Orionis E: (Purple) Rim, (Orange) Center, (Teal) Front. (Center):  $\lambda$  Orionis W: (Orange) Body, (Blue) Front and back legs, (Green) Wings, (Pink) Spine. (Right):  $\lambda$  Orionis S: (Purple) Head, (Cyan) Legs, (Pink) High-velocity cloud.

mass of the hydrogen atom.  $\kappa$  is often assumed to be constant over an entire field, with  $\kappa_0 = 0.1 \text{ cm}^2 \text{ g}^{-1}$  at 1000 GHz (Beckwith et al. 1990) being used in many studies (e.g. Alina et al. 2022; Mannfors et al. 2021). In BFROST-I we calibrate for the known variation in dust opacity, following Lewis et al. (2022), with a method first introduced by Lombardi et al. (2014).  $N(\text{H})$  can be related to K-band extinction  $A_K$  with  $N(\text{H}) = \beta_K A_K$ , where  $\beta_K = 1.67 \times 10^{22} \text{ cm}^{-2} \text{ mag}^{-1}$  (Bohlin et al. 1978; Savage & Mathis 1979) and  $A_K/A_V = 0.112$ . We then fit a linear relation between optical depth at 353 GHz  $\tau_{353}$  and  $A_K$  of  $A_K = \gamma \tau_{353} + \delta_K$ . The value of  $\kappa_0$  can be estimated from  $\gamma$  with

$$\kappa_{353} = 1/(\mu_H m_H \beta_K \gamma) \quad \text{where } \mu_H = 1.37 \text{ is the gas mass per hydrogen atom. In BFROST-I we determined } \kappa_0 = 8.8 \times 10^{-3} \text{ cm}^2 \text{ g}^{-1} \text{ at 353 GHz for E.}$$

We have used Planck optical depth  $\tau_{353\text{GHz}}$  maps to estimate column density at a resolution of  $5'$  using

$$N(\text{H}_2) = N_P = \frac{\tau_{353\text{GHz}}}{\kappa_\nu \mu m_H}. \quad (6)$$

We refer to these maps using the notation  $N_P$ . For W and S, column densities are always at the Planck resolution. The higher-resolution *Herschel* data in E allow us to compare the Meissa-facing Head and more shielded Rim in more detail. We fit Eq. 4

to *Herschel* SPIRE 250, 350, and 500  $\mu\text{m}$  maps to calculate dust properties at a resolution of  $\sim 36''$ , referring to these with the notation  $N_{\mathcal{H}}$ . When not otherwise specified in the text or caption, we denote properties calculated with *Herschel* column densities with a subscript of  $\mathcal{H}$  and those with Planck  $N(\text{H}_2)$  with  $\mathcal{P}$ .

### 3.4. Estimation of CO column density

Estimation of local thermodynamic equilibrium (LTE) and non-LTE CO column densities is explained in more depth in BFROST-I. We divided our maps into regions, with Mask 1 referring to a significant ( $T_{\text{MB}} > 5\sigma_{\text{RMS}}$ ) detection of both  $^{12}\text{CO}$  and  $^{13}\text{CO}$  and Mask 2 to those regions with only significant  $^{12}\text{CO}$  detection. In Mask 1 we assume LTE, calculated excitation temperature  $T_{\text{ex}}$  from the peak of the  $^{12}\text{CO}$  spectrum, and assumed that the  $^{12}\text{CO}$  and  $^{13}\text{CO}$  lines have the same  $T_{\text{ex}}$  (Pineda et al. 2010; Mangum & Shirley 2015). We estimated the optical depth from the  $^{13}\text{CO}$  line and used this to calculate the optical depth of the  $^{12}\text{CO}$  line. For the  $^{12}\text{CO}$ -to- $^{13}\text{CO}$  ratio we used ratios estimated from simulations by Szűcs et al. (2014).

Regions without significant  $^{13}\text{CO}$  signal cannot be assumed to be in LTE. Instead, we reproduced the method used by Goldsmith et al. (2008); Pineda et al. (2010). We divided the  $T_{\text{ex}}$  maps of the sources into bins of 1 K, and calculated line ratios  $^{12}\text{CO}/^{13}\text{CO}$  using the mean spectrum per bin. We then performed non-LTE radiative transfer calculations using RADEX (van der Tak et al. 2007) using fixed kinetic temperature  $T_{\text{kin}} = 15$  K. Total CO column density per linewidth  $N(\text{CO})/\delta\nu$ , number density  $n(\text{H}_2)$ , and the abundance ratio  $R$  of  $^{12}\text{CO}$  and  $^{13}\text{CO}$  were set as free parameters. We derived a powerlaw relation between  $T_{\text{ex}}$  and  $N(\text{CO})/\delta\nu$ , calculating a  $N(\text{CO})$  map from the  $T_{\text{ex}}$  map multiplied by the linewidth. In Mask 1 regions the LTE and non-LTE maps were combined and in Mask 2 regions we directly used the non-LTE method to derive the final  $N(\text{CO})$  map. In this paper, we use this combined non-LTE  $N(\text{CO})$  map for analysis.

### 3.5. X-factors

The conversion factor between CO and  $\text{H}_2$ ,  $X(\text{CO})$ , is often used to estimate  $\text{H}_2$  column densities in extragalactic studies. Bolatto et al. (2013) have estimated a value of  $X_{\text{Gal}} = 2 \times 10^{20} \text{ cm}^{-2} (\text{K km s}^{-1})^{-1}$  for the  $^{12}\text{CO}(J = 1 - 0)$  line in the Milky Way. However, X factor has been shown to vary within the Galaxy and within clouds due to abundances, the UV radiation field, and metallicity. The X-factor is defined as

$$X \equiv \frac{N(\text{H}_2)}{W(\text{CO})}, \quad (7)$$

where  $W$  is the zeroth-moment (integrated intensity) map of  $^{12}\text{CO}$  or  $^{13}\text{CO}$ . We calculated X-factor for E using *Herschel* data convolved to the TRAO resolution ( $X_{\mathcal{H}}$ ). For S, which does not have *Herschel* data, the  $W(^{12}\text{CO})$  and  $W(^{13}\text{CO})$  maps were convolved and reprojected to the Planck resolution ( $X_{\mathcal{P}}$ ).  $X_{\mathcal{P}}$  was also calculated for E for comparison, but we use  $X_{\mathcal{H}}$  in analysis. In this publication X-factor refers specifically to the CO X-factor.

## 4. Results

### 4.1. Large-scale morphology and the B-field

We detected anticorrelation between polarization angle  $p$  and both  $N_{\mathcal{P}}$  and  $N_{\mathcal{H}}$  column densities in all fields. For the full TRAO field we detected polarization fractions of 6.8%, 4.0%,

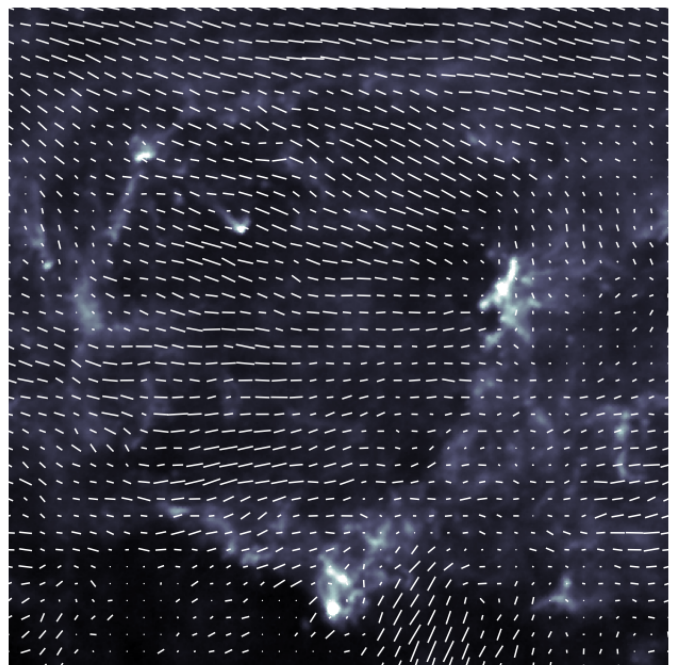


**Fig. 5.** The *Planck* magnetic field overplotted on the *Planck* 353 GHz intensity map. The size of the marker corresponds to polarization fraction.

and 6.6% for E, W, and S, respectively. Polarization fraction in the Rim in E is  $4.7^{+4.8}_{-3.6}\%$  and in the Front is  $5.1^{+7.3}_{-3.8}\%$ . High polarization fractions of  $\sim 10\%$  can be detected within the H II region beyond the E cloud in the direction toward Meissa. The B-field in the H II region surrounding Meissa is parallel to the Galactic plane (Fig. 5). In the Northern rim of the ring the B-field traces the molecular gas.

We show the results of FilDReAMS fitting in Figs. C.1-C.3. Frame (a) shows the B-fields over the individual clouds. In E, the mean B-field angle is tilted  $\sim 45^\circ$  with respect to the direction of the long axis of the cloud and is mostly well-ordered. Individual filaments are not well-aligned with the B-field, but are rather aligned better with the direction of radiation from Meissa. In W, the B-field seems to trace the dense Spine, but behind the cloud becomes more disorganized. In the dense Head of S, the B-field seems to form a loop.

Maximum filament width (frames b-c) is smallest in E due to the shape of the map; in both S and W the largest detected filament widths are  $\sim 0.5$  pc.  $W_{\text{b,max}}$  in the Rim of E is larger than that in the Front by around 0.05 pc. Frames d-f show maps of  $\Delta\Psi$ . We detect filaments that are parallel and those that are perpendicular to the B-field in the same regions and at the same scales without any noticeable global alignment. In frames h-j we plot  $\Delta\Psi$  as a function of  $W(^{12}\text{CO})$ . Overall, the filaments in  $\lambda$  Orionis are somewhat more perpendicular to the B-field at low  $W(^{12}\text{CO})$  and parallel at high  $W(^{12}\text{CO})$ , however this trend is not significant. This correlation is strongest in the W cloud (frame i), where filaments at  $W(^{12}\text{CO}) \geq 10 \text{ K km s}^{-1}$  are approximately parallel to the B-field. At small scales however we detect no correlation between  $\Psi_{\text{f}}$  and  $\Psi_{\text{B}}$  in any of the fields.

### 4.2. Structure of the subregions

The dendrogram tree diagrams in Fig. 4 show the complexity of each subregion, as well as how they are connected above the

baseline emission. A trunk refers to the base structure of a dendrogram region, a branch is any structure that is not a trunk, and leaves are top-level structures. The same figure also shows the spatial extent of the subregions.

The dendrogram structure of E is the simplest of the clouds. It is composed of three regions: the compact Front, the Rim which lies along the  $\lambda$  Orionis ring, and the diffuse Center between the Front and the Rim. The Front is one single tree, whereas the Rim and Center are composed of multiple trees in both CO isotopologs. The Rim covers three trunks with substructure in  $^{12}\text{CO}$  and two in  $^{13}\text{CO}$ . Other than a few peaks in  $^{13}\text{CO}$  in the Rim, the Front dendrogram regions have the highest intensity.

W is a complex structure in PPV space. However the  $^{13}\text{CO}$  dendrogram is segmented partly due to the poor baseline (Appendix A). Though we show the dendograms, the structure of the Body and Wings in  $^{13}\text{CO}$  are not used in analysis. The Body is a single tree in  $^{12}\text{CO}$ , containing the Legs and Spine as well as parts of the Wings. The Spine is a dense filament located in the Body and is a unified substructure in both isotopologs. The Wings cover multiple individual trees as well as branches within the Body. The Front and Back legs are two overlapping structures at significantly different velocities, but in  $^{12}\text{CO}$  are still connected in velocity space to the Body. The Back Leg is at  $v_{\text{cen},12\text{CO}} \sim 13.3 \text{ km s}^{-1}$ , and the Front Leg is at  $v_{\text{cen},12\text{CO}} \sim 8.8 \text{ km s}^{-1}$ , closer in velocity to the rest of W.

In S, the Head and High-Velocity Cloud are one structure each, whereas the Legs are composed of multiple trees. We further refer to the largest base-level dendrogram in S as the Body; this includes the Head and part of the Legs. The High-Velocity Cloud is not detected in  $^{13}\text{CO}$ , and thus is possibly a lower-density structure.

We show the spectra of the subregions in Fig. 6. In E, the Front has a single-peaked spectrum with higher intensity than the Rim, whereas the Rim has two main peaks at  $v_{\text{cen}} \approx 9, 11 \text{ km s}^{-1}$ . The Center peaks at a similar  $v_{\text{cen}}$  to the Front, with a second shallow peak at  $14 \text{ km s}^{-1}$  but has sum of  $T_A$  integrated over the structure about ten times lower than the Front or Rim. In W, the Body is Gaussian in shape with a long tail extending to higher velocity. Despite their multiple structures, the Wings are fairly Gaussian in shape as well, with a second clear peak at  $\sim 3 \text{ km s}^{-1}$ . Both Legs and the Spine are Gaussian in shape with one peak. In S, the Head is double-peaked, but the legs are composed of at least three main Gaussian peaks. The High-Velocity Cloud also seems to be a sum of two gaussians.

#### 4.3. Dust properties

##### 4.3.1. Estimates of $N(\text{H}_2)$

We show maps of  $N(\text{H}_2)$  in Fig. D.1. Mean  $\text{H}_2$  column density at Planck resolution in E is  $(5.44 \pm 3.68) \times 10^{20} \text{ cm}^{-2}$ , and in S is  $(7.45 \pm 4.92) \times 10^{20} \text{ cm}^{-2}$ , reaching up to a few times  $10^{22} \text{ cm}^{-2}$  in the densest regions in both fields. Using MBB fitting (Sect. 3.3) to *Herschel* data, we estimate the dust temperature  $T$ , spectral index  $\beta$ , optical depth  $\tau$ , and  $N(\text{H}_2)$  (Table 2) and plot maps of  $T$  and  $N(\text{H}_2)$  with  $N(\text{CO})$  contours at the TRAO resolution in Fig. 7. Dust temperature is higher in the Front by  $\sim 2 \text{ K}$ , and in the map a region of  $T \geq 20 \text{ K}$  can be seen at the Meissa-facing head of the Front, with a colder filamentary center. Though column densities in both regions have a similar order of magnitude, such high temperatures are not visible in the Rim region. The distribution of dust temperatures in the Front is also wider than in the Rim. It is not surprising that  $N(\text{CO})$  and  $N(\text{H}_2)$  show spatial

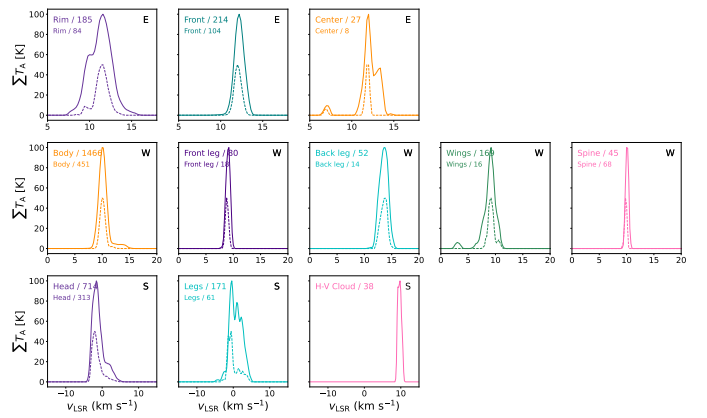


**Fig. 6.** Normalized spectra in  $^{12}\text{CO}$  (solid lines) and  $^{13}\text{CO}$  (dashed lines) for each dendrogram subregion in each field. The top normalization factor in each frame corresponds to the value for  $^{12}\text{CO}$ , and the bottom to  $^{13}\text{CO}$ . These figures show the sum of emission in each region using only pixels within the dendrogram datacube. H-V Cloud stands for the High-Velocity Cloud, and does not have emission in  $^{13}\text{CO}$ . The x-axis has the same range in each row.

correlation, or that  $N(\text{CO})$  and temperature are anticorrelated. However, in both the Front and Rim,  $N(\text{CO})$  increases steeply in the regions facing Meissa. In the trailing region, CO contours decrease more gradually, showing compression of gas due to high UV pressure. The region of highest temperature in the Front is located just outside the CO contours.

The probability density functions (PDFs) of  $N_P$  and  $N_H$  are shown in Fig. 8. As with MBM12 in BFROSTII, we find peak column densities approximately an order of magnitude higher with *Herschel* data. Part of this discrepancy in  $N(\text{H}_2)$  is due to the dust temperatures used to estimate column densities, as *Planck* temperatures are around 5.4 (4.1) K larger for the Front (Rim) regions. Both *Herschel* PDFs show a powerlaw tail between  $\log(N_H) \approx 21 - 22.5 \text{ cm}^{-2}$ . The Front has a slight double-peaked structure and the Rim a single peak. The PDF of the Front at *Planck* resolution also shows a slight double-peaked structure but the Rim does not show a power-law decrease at all. Column density across the Planck fields does not vary as much as it does in the *Herschel* data since small-scale variations are not visible at the *Planck* resolution.

We further show PDFs of the *Planck*  $N(\text{H}_2)$  for all three fields in Fig. 9. In  $N_P$ , E has a single peak with a powerlaw tail. The peak of W is more broad, but also shows a powerlaw tail and a second small peak at  $\log(N_P) \sim 21.2 \text{ cm}^{-2}$ . The PDF of S has a multi-peaked structure with a less clear powerlaw tail.

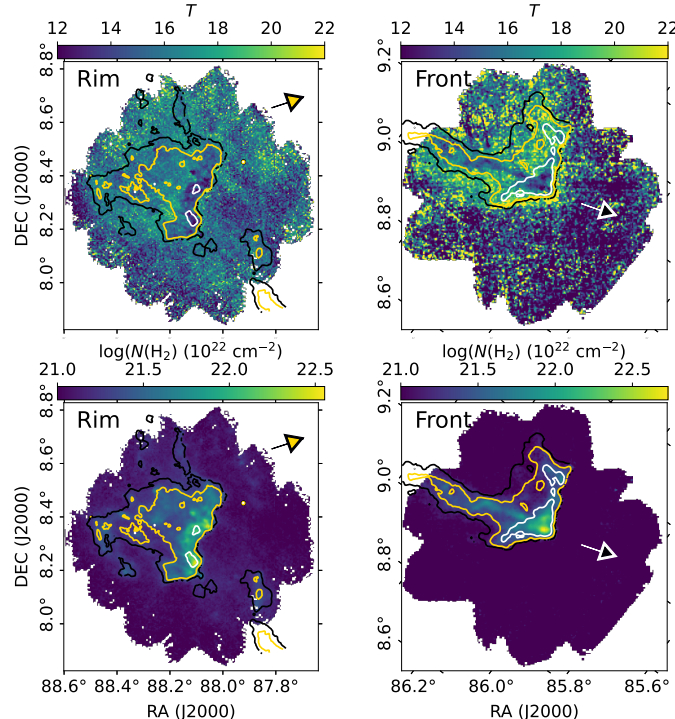
The PDFs of MCs can be fitted with a log-normal distribution, but deviations at high or low  $N$  are to be expected if the equation of state is not isothermal or due to self-gravity (Paszot & Vázquez-Semadeni 1998; Scalo et al. 1998; Ostriker et al. 2001; Vázquez-Semadeni & García 2001; Tassis et al. 2010; Pineda et al. 2010). Figure 10 shows the normalized PDF of extinction from the 2' iNICEST map. Following Pineda et al. (2010) we fit the PDFs with a Gaussian of the form

$$f(\ln(x)) = N_{\text{pix}} \exp \left[ -\frac{(\ln(x) - \langle \ln(x) \rangle)^2}{2\sigma(\ln(x))^2} \right]; x \equiv \frac{N}{\langle N \rangle} \quad (8)$$

where  $\sigma(\ln(x))^2$  is the variance of  $x$ , and  $N$  is either the column density or extinction. All three fields have long tails at low  $A_v$  but are otherwise Gaussian in shape.

**Table 2.** Dust parameters of MBB fitting using *Herschel* data.

Region	Mask	$T$ (K)	$N(\text{H}_2)$ ( $10^{21} \text{ cm}^{-2}$ )	$\beta$	$\tau$ ( $10^{-4}$ )
Front	$^{12}\text{CO}$	$17.7^{+5.8}_{-4.4}$	$2.2^{+3.1}_{-1.4}$	$1.7^{+0.6}_{-0.6}$	$8.7^{+14.2}_{-7.3}$
Rim	$^{12}\text{CO}$	$15.7^{+3.4}_{-2.8}$	$2.2^{+2.8}_{-1.1}$	$1.8^{+0.5}_{-0.5}$	$9.0^{+10.3}_{-6.2}$
Front	$^{13}\text{CO}$	$17.7^{+5.4}_{-3.9}$	$2.7^{+4.0}_{-1.8}$	$1.7^{+0.5}_{-0.6}$	$10.6^{+17.5}_{-8.8}$
Rim	$^{13}\text{CO}$	$15.8^{+2.7}_{-2.4}$	$3.0^{+4.9}_{-1.5}$	$1.8^{+0.4}_{-0.4}$	$11.5^{+15.2}_{-7.3}$

**Table 3.** Derived mean  $\pm$  (95th, 5th percentile) values from MBB fitting, assuming  $\kappa_0 = 8.8 \times 10^{-3} \text{ cm}^2 \text{ g}^{-1}$  and with a variable  $\beta$ . These values include only pixels within the corresponding dendrogram subregion masks, which are drawn in Fig. 4.**Fig. 7.** Results of MBB fitting. (Top) Dust temperature and (bottom)  $N(\text{H}_2)$  for the Front (right) and Rim (left) regions. The contours are from the  $N(\text{CO})$  maps at levels of  $3 \times 10^{16}$ ,  $1 \times 10^{17}$ , and  $4 \times 10^{17} \text{ cm}^{-2}$ . The colorbars are the same for the Front and Rim regions to facilitate comparison.

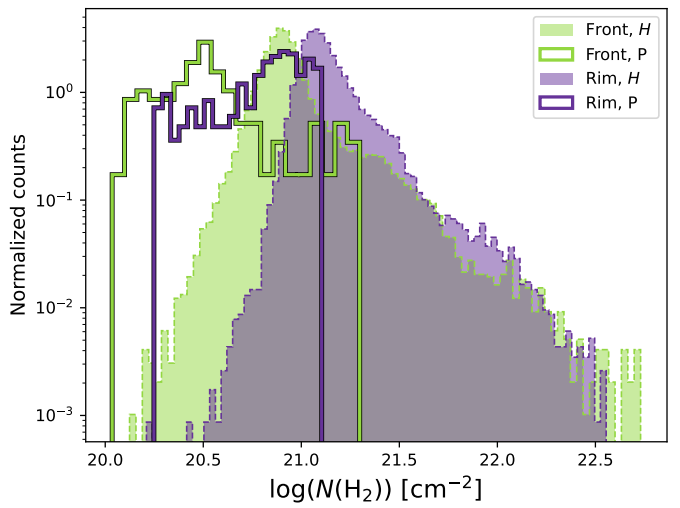
#### 4.3.2. CO

Maps of  $N(\text{CO})$  are also shown in Fig. D.1. Mean  $N(\text{CO})$  in E is  $(0.82 \pm 1.32) \times 10^{17} \text{ cm}^{-2}$  and in S is  $(1.11 \pm 1.58) \times 10^{17} \text{ cm}^{-2}$ . The Front in E has higher  $N(\text{CO})$  than the Rim, at mean values of  $(1.3 \pm 1.94)$  and  $(0.7 \pm 0.84) \times 10^{17} \text{ cm}^{-2}$ , respectively. Likewise, in S the Head is more dense than the Legs at  $N(\text{CO}) \approx (1.65 \pm 1.86)$  and  $(0.58 \pm 0.72) \times 10^{17} \text{ cm}^{-2}$ .

PDFs of  $N(\text{CO})$  are shown in Fig. 11. In CO, both E and S show one peak at  $N(\text{CO}) \sim 10^{15} \text{ cm}^{-2}$  and another near  $N(\text{CO}) \sim 10^{17}$  with a power-law decrease after  $10^{17} \text{ cm}^{-2}$ .

#### 4.4. $N(\text{H})$ from HI4PI

The CO  $\lambda$  Orionis ring is located at the edge of the H $\text{i}$  bubble around Meissa. Contours of H $\text{i}$  column density follow the rim of the bubble observed in *Planck*  $N(\text{H}_2)$ . Contour maps of the integrated intensity of H $\text{i}$  trace the extent of  $W(^{12}\text{CO})$  especially

**Fig. 8.** PDFs of  $N(\text{H}_2)$  for E using *Herschel* (colored histograms) and Planck (outlines). The Rim is shown in darker purple and the Front in lighter green. The  $N_p$  data use only those pixels which correspond to  $N_h$  data.

in W and S (Fig. 12). As the resolution of the HI4PI data is low ( $16.2'$ ), more detailed correlation of  $W(\text{CO})$  and  $W(\text{H}\text{i})$  is not possible.

#### 4.5. X-factor

We show maps of  $W(^{12}\text{CO})$  and  $W(^{13}\text{CO})$  used to calculate  $X(\text{CO})$  for E and S in Fig. D.1 (frames i-l). Mean X-factors for each field and subregion are shown in Table 4, with the spatial distribution of X shown in Fig. 13. X-factors derived using *Herschel* column densities ( $X_h$ ) are a factor of 10 higher than those derived with Planck column density ( $X_p$ ).  $X(^{13}\text{CO})$  is around 4–12 times larger than  $X(^{12}\text{CO})$  in each field. X is highest at the edges of the cloud in a band less than the size of one TRAO beam and decreases inside the cloud. The extent of  $X_h(^{13}\text{CO})$  is different from that of the  $X_h(^{12}\text{CO})$  only on the cloud edges shielded from Meissa. In the Meissa-facing regions of both the Rim and Front the extent of both  $^{12}\text{CO}$  and  $^{13}\text{CO}$  are nearly identical, whereas the tail end of the Head and Rim are more extended in  $^{12}\text{CO}$  than  $^{13}\text{CO}$  (note that the sharp cutoff at the trailing end of the Head is due to the limited extent of the *Herschel* data). In a MC one would expect a shell of  $^{12}\text{CO}$  surrounding a denser region in which both  $^{12}\text{CO}$  and  $^{13}\text{CO}$  are detected. Instead the Meissa-facing edges of the cloud show a highly-compressed region in which the transition from atomic carbon to CO occurs nearly instantaneously. CO depletion is clearly seen in the dense filament and core within the Front. In  $^{12}\text{CO}$  we detect several possible CO-depleted cores at the head of the Front. Even  $^{13}\text{CO}$  appears to become optically thick in the center of this filament and in two cores. The Meissa-facing edge of the Rim also shows CO depletion and one dense core. At the Planck resolution in S we do not detect  $^{12}\text{CO}$  depletion within the dense cores.

We show PDFs of  $X_h$  for E and  $X_p$  for S in Fig. 14. In E, both  $^{12}\text{CO}$  and  $^{13}\text{CO}$  have long tails of low X and the X-distributions of the two isotopologs have similar shapes. There is a powerlaw decrease in the range  $X \sim 10^{20} - 10^{21}$ , and a second peak in the PDF at around  $X \sim 10^{21}$  in  $^{12}\text{CO}$  and  $X \sim 10^{22}$  in  $^{13}\text{CO}$ . The PDFs of the subregions are also fairly similar in shape and have similar mean X-factor. In S,  $X(^{12}\text{CO})$  is under

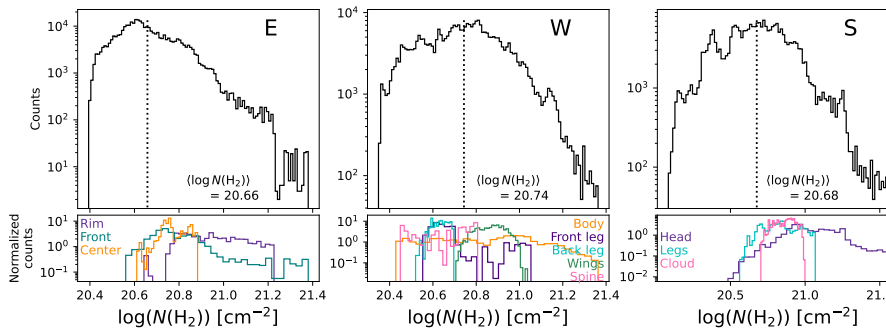


**Fig. 9.** PDF of  $N(\text{H}_2)$  at Planck resolution. The top frames show the full field, and the bottom frames the PDFs of the subregions. Dotted vertical lines mark the mean value over the full field.

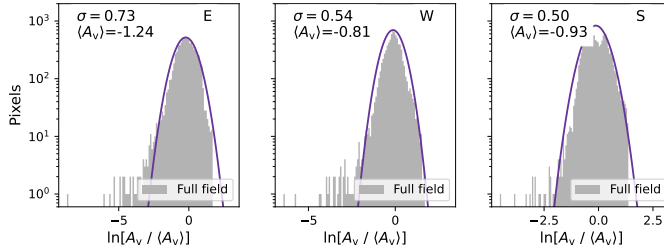


**Fig. 10.** Normalized PDF of extinction. The solid lines show the Gaussian fits to the histogram as in Pineda et al. (2010). The standard deviation  $\sigma$  and logarithm of mean column density are written on the frames.

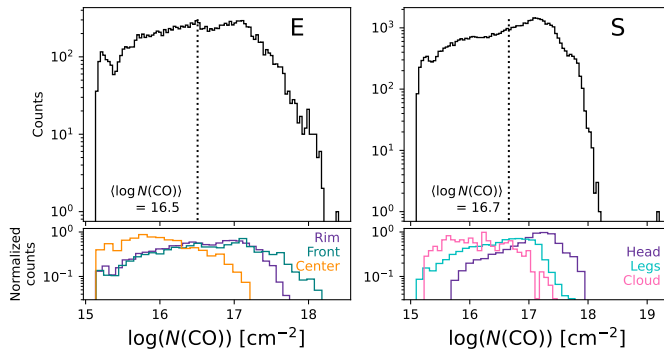


**Fig. 11.** PDF of  $N(\text{CO})$  at TRAO resolution for E and S. The top frames show the full field, and the bottom frames show the PDFs of every subregion. Dotted vertical lines mark the mean value over the full field.

$\sim 10^{20.5}$ , but  $X(^{13}\text{CO})$  can reach above  $10^{28}$ . In S as well we do not detect significant differences between the subregions.

#### 4.6. Abundances

The abundance  $[\text{CO}/\text{H}_2]$  represents the ratio of column densities  $N(\text{CO})/N(\text{H}_2)$ . Using  $N_{\mathcal{H}}$  the abundance is of the order of  $10^{-5}$ , with  $N_{\mathcal{P}}$  it is a factor of 10 higher. As  $N_{\mathcal{H}}$  column densities are a factor of 10 larger than  $N_{\mathcal{P}}$  column densities this is to be expected. The mean  $[\text{CO}/\text{H}_2]$  in E with  $N_{\mathcal{H}}$  is  $3.7^{+6.7}_{-3.7} \times 10^{-5}$  and with  $N_{\mathcal{P}}$  in S is  $2.0^{+2.7}_{-1.6} \times 10^{-4}$ .

The spatial distribution of abundance and fits to the full field and subregions are shown in Fig. 15. In E, in the Meissa-facing edge of the Head the abundance is significantly higher than anywhere else in the regions, at around  $2 \times 10^{-4}$ . Similar peaks in abundance are not observed in the Rim. The mean abundance ratio in the Front is twice that of the Rim, at  $(5.6 \text{ and } 2.9) \times 10^{-5}$ , respectively. The full field histogram in  $N_{\mathcal{H}}$  shows a double slope; when plotting the Rim and Head separately, it is clear that the

**Table 4.** X-factor for the full field and subregions.

Field	X-factor ( $10^{20} \text{ cm}^{-2} \text{ km}^{-1} \text{ s K}^{-1}$ )				
E ( $X_{\mathcal{H}}$ )	All	Rim	Front		
	$^{12}\text{CO}$	$3.4^{+11.0}_{-2.7}$	$3.9^{+14.1}_{-3.1}$	$2.4^{+5.0}_{-1.8}$	
	$^{13}\text{CO}$	$14.8^{+40.0}_{-10.3}$	$17.4^{+44.1}_{-12.1}$	$10.8^{+24.7}_{-6.9}$	
	$\Delta X$	4.35	4.46	4.50	
E ( $X_{\mathcal{P}}$ )	All	Rim	Front	Center	
	$^{12}\text{CO}$	$0.4^{+0.4}_{-0.3}$	$0.5^{+0.3}_{-0.3}$	$0.3^{+0.3}_{-0.2}$	$0.4^{+0.1}_{-0.1}$
	$^{13}\text{CO}$	$2.7^{+4.4}_{-2.6}$	$3.6^{+4.8}_{-2.5}$	$1.5^{+2.7}_{-1.4}$	$2.4^{+1.3}_{-0.9}$
	$\Delta X$	6.75	7.2	5.0	6.0
S ( $X_{\mathcal{P}}$ )	All	Head	Legs	Cloud	
	$^{12}\text{CO}$	$0.5^{+0.5}_{-0.3}$	$0.5^{+0.4}_{-0.3}$	$0.5^{+0.6}_{-0.4}$	$0.9^{+0.5}_{-0.3}$
	$^{13}\text{CO}$	$3.9^{+6.1}_{-2.7}$	$3.7^{+5.5}_{-2.5}$	$4.2^{+7.0}_{-3.3}$	$10.7^{+8.8}_{-4.7}$
	$\Delta X$	7.8	7.4	8.4	11.89

**Notes.** The difference  $\Delta X$  is calculated as  $X(^{13}\text{CO})/X(^{12}\text{CO})$ . We use the  $^{12}\text{CO}$  dendrogram regions to calculate both  $X(^{12}\text{CO})$  and  $X(^{13}\text{CO})$  and thus the values of both isotopologs represent the same number of map pixels.

Rim has a slope around half that of the Front. While the Front has slightly lower range in  $N_{\mathcal{H}}$ , it reaches significantly higher  $N(\text{CO})$ . The slope for the Front is also highest of the E subregions in  $N_{\mathcal{P}}$ .

At the Planck resolution, we do not detect depletion in S. As the resolution of Planck corresponds to  $\sim 0.6 \text{ pc}$  at the distance of  $\lambda$  Orionis, we do not expect to detect anything at scales below that of large clumps.

#### 4.7. Environmental classification

To characterize the  $\lambda$  Orionis regions we compare  $T_{\text{ex}}$ ,  $X(^{12}\text{CO})$ ,  $X(^{13}\text{CO})$ ,  $W(^{12}\text{CO})$ ,  $W(^{13}\text{CO})$ ,  $N(\text{CO})$ ,  $[\text{CO}/\text{H}_2]$ , and  $N(\text{H}_2)$ . We show scatterplots of these parameters at the TRAO resolution in E in Fig. 4.7 and the same for S at the  $N_{\mathcal{P}}$  resolution in Fig. E.

There is larger scatter in  $X_{\mathcal{H}}$  of both isotopologs at lower  $T_{\text{ex}}$  and a second peak in scatter at  $T_{\text{ex}} \sim 25 \text{ K}$  (frames a, b). Higher  $T_{\text{ex}}$  also corresponds to larger scatter in abundance (frame c), but abundance also clearly correlates with  $N(\text{CO})$ . As seen in Fig. 15, column densities of CO and  $\text{H}_2$  are approximately linearly correlated. In contrast, abundance does not seem to correlate with  $N_{\mathcal{H}}$  (frame d) but higher abundance correlates with higher  $T_{\text{ex}}$ .  $N_{\mathcal{H}}$  does correspond to larger  $W(\text{CO})$  in both isotopologs (frames e, f). There are clear cutoff points in the plots of  $N(\text{CO})$  against  $X_{\mathcal{H}}$ , especially with  $X_{\mathcal{H}}(^{13}\text{CO})$  (frames g, h). There is larger scatter in  $X_{\mathcal{H}}(^{12}\text{CO})$  at higher  $N(\text{CO})$ . We detect saturation of  $^{12}\text{CO}$  at around  $X_{\mathcal{H}}(^{12}\text{CO}) \sim 30X_{\text{Gal}}$  (frame i). Abundance and  $X_{\mathcal{H}}(^{12}\text{CO})$  are approximately correlated up

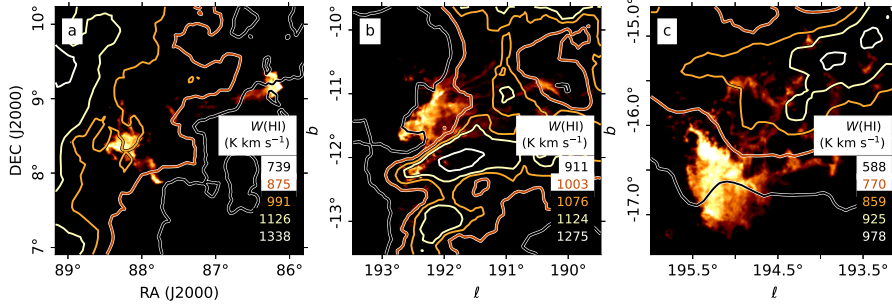


**Fig. 12.** Contours of  $W(\text{H I})$  drawn on top of the  $W(^{12}\text{CO})$  maps. The intensity of each contour is written on the image in units of  $\text{K km s}^{-1}$ , with darker colors corresponding to lower  $W(\text{H I})$ .

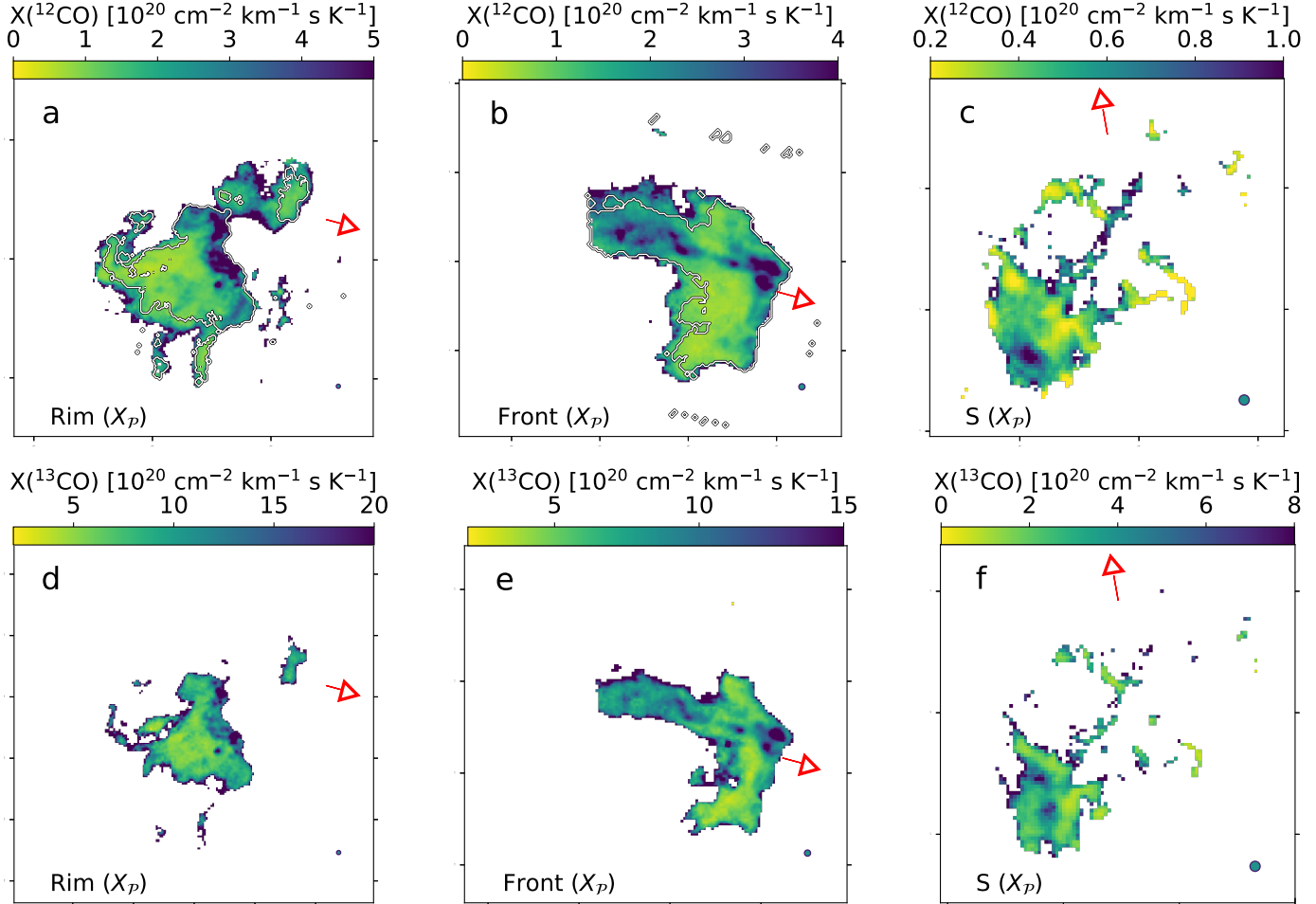


**Fig. 13.** X-factors. (a)  $X(^{12}\text{CO})$  for the Rim in E using the  $N_{\text{H}}$  and  $W(^{12}\text{CO})$  at TRAO resolution. (b)  $X(^{12}\text{CO})$  for the Front in E using the  $N_{\text{H}}$  and  $W(^{12}\text{CO})$  at TRAO resolution. (c)  $X(^{12}\text{CO})$  of S using  $N_{\text{p}}$  and  $W(^{12}\text{CO})$  at Planck resolution. (d-f) Same as the upper row but for  $X(^{13}\text{CO})$ . The red arrows point in the direction of Meissa. The beam is shown in the lower right.

to this point; after this  $X_{\mathcal{H}}(^{12}\text{CO})$  remains constant. While an upper limit to abundance- $X_{\mathcal{H}}(^{13}\text{CO})$  is also visible, we do not detect this saturation cutoff (frame l). Using *Herschel*, column density and X-factor show a doubly-peaked structures (frames j, k). There is a clear cutoff around  $N_{\text{H}} \sim 2 \times 10^{21} \text{ cm}^{-2}$ , but with  $X_{\mathcal{H}}$  increasing again after this point in both  $^{12}\text{CO}$  and  $^{13}\text{CO}$ . We compare  $A_{\text{v}}$  and X-factor in Fig. 17 (see Fig. 6 in Szűcs et al. 2016).

Szűcs et al. (2016) analyzed hydrodynamical simulations of MCs in a variety of environments. For the relation between  $A_{\text{v}}$

and X, they use

$$X_{\text{CO}} = \begin{cases} X_{\text{Gal}} \left( \frac{\langle A_{\text{V}} \rangle}{3.5} \right)^{-3.5} & \text{if } A_{\text{V}} < 3.5 \text{ mag} \\ X_{\text{Gal}} & \text{if } A_{\text{V}} \geq 3.5 \text{ mag}. \end{cases} \quad (9)$$

To understand the environment of  $\lambda$  Orionis we perform this fitting to our data. We show these fits with solid black lines in Fig. 17; these relations generally do not fit the data. We show another fit, replacing  $X_{\text{Gal}}$  with the peak of the histogram of X. Further, the limit of  $A_{\text{v}} = 3.5$  mag is set to the peak of the  $A_{\text{v}}$  histogram. The limit of  $A_{\text{v}}$  is 1.4, 1.0, and 0.5 mag in  $X(^{12}\text{CO})$  for E Rim, E Front, and S, respectively. In  $^{13}\text{CO}$  these values are 1.8, 1.3, and 0.5 mag, respectively. For the second peak at

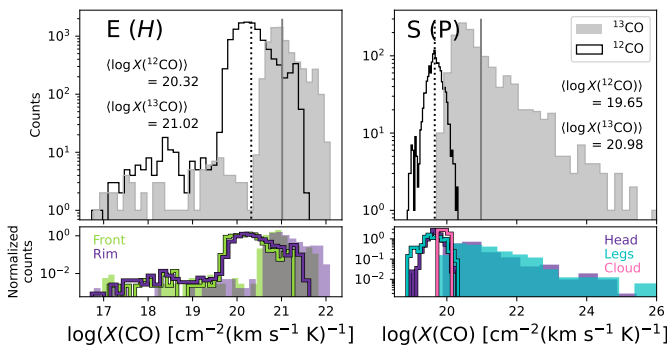


**Fig. 14.**  $X(^{12}\text{CO})$  (outlines) and  $X(^{13}\text{CO})$  (colored histogram) for E at *Herschel* resolution and S at Planck resolution. The extent of the  $X_H(^{13}\text{CO})$  data are marked with white contours on the  $X_H(^{12}\text{CO})$  map. Dotted vertical lines mark the mean value of  $X(^{12}\text{CO})$  and solid gray vertical lines the mean  $X(^{13}\text{CO})$  over the full field.

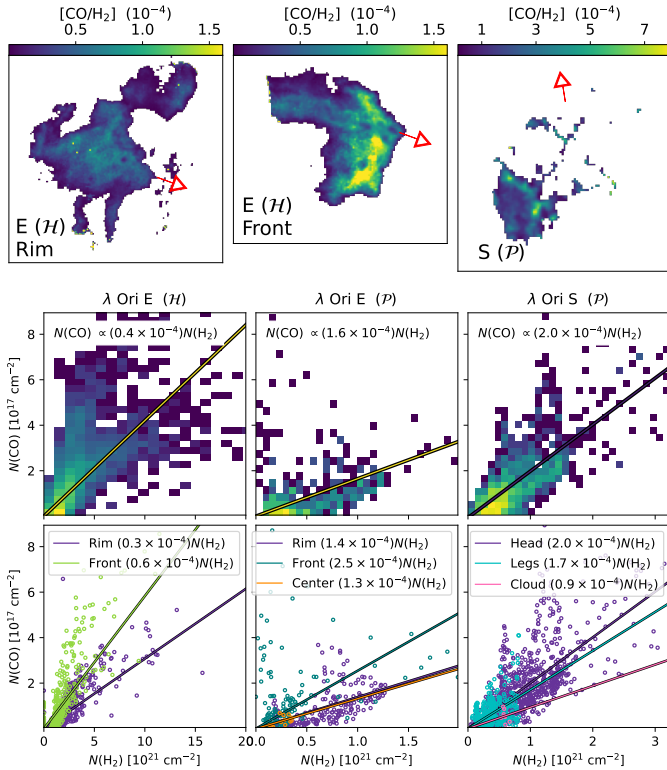


**Fig. 15.**  $[\text{CO}/\text{H}_2]$  abundances for E using  $N_H$  and  $N_P$ , and for S using  $N_P$ . (top) Map of abundance. (middle) Histograms of  $N(\text{H}_2)$  against  $N(\text{CO})$  for the full field. The linear fit is plotted on top, with the slope printed on the frame. (bottom): The same as the middle, but for sub-regions. We plot every tenth datapoint for the  $N_H$  abundances but use every pixel for fitting.

0.4  $X_{\text{Gal}}$  in E Front, the extinction limit is 1.3 mag. We see low X-factor compared to  $X_{\text{Gal}}$ , but also a lower limit for  $A_v$ . We detected an extinction threshold of  $\sim 1$  mag for  $^{12}\text{CO}$  and  $^{13}\text{CO}$ , consistent with the literature (Visser et al. 2009; Roueff et al. 2021).

Due to its lack of *Herschel* data, we do not resolve small-scale physics in S. There is a slight decrease in  $X_P(^{12}\text{CO})$  with increasing  $T_{\text{ex}}$  but  $X_P(^{13}\text{CO})$  is practically constant across the range of  $T_{\text{ex}}$  (frames a, b). Excitation temperature and abundance are correlated, with larger scatter above  $T_{\text{ex}} \geq 12$  K (frame c).  $N_P$  is fairly well correlated with  $N(\text{CO})$ , as are  $W(^{12}\text{CO})$  and

$W(^{13}\text{CO})$  (frames e, f). The low abundance compared to  $X_{\text{Gal}}$  is clear in frames e-f. As with E,  $N_P$  and abundance do not show correlation (frame d). The cutoff point in  $N(\text{CO})$ - $X_P(^{12}\text{CO})$  is visible, but is quite unclear in  $X_P(^{13}\text{CO})$  (frames g, h). Abundance and X-factor have an approximately linear relation though there is a slight plateau at  $X_P(^{12}\text{CO}) \sim 38 X_{\text{Gal}}$  at  $[\text{CO}/\text{H}_2] \leq 2.5$  (frames i, l). We note an upper limit between  $N_P$  and  $X_P(^{12}\text{CO})$  (frame j). A similar double slope to that in E is visible, but with larger scatter than at TRAO resolution. This slope is not seen in  $^{13}\text{CO}$ , where  $X_P(^{13}\text{CO})$  is fairly constant across the range of  $N_P$  (frame k). In Fig. 17, we detect  $^{12}\text{CO}$  saturation. However,  $^{13}\text{CO}$  shows no relation at all. Due to the lower resolution of Planck data, all values are shifted to lower  $A_v$ .

Correlation scatterplots between individual subregions are shown in Fig. 18. We detect similar trends between the properties in both E and S. The data are consistent with Larson's relations (Larson (1981); frames a and b).

#### 4.8. Gravitational stability and analysis of dendograms

Frames c and d in Fig. 18 show trends between virial parameter  $\alpha_{\text{vir}}$ , effective radius, and velocity dispersion of structures in  $^{13}\text{CO}$ . In general, larger structures also have lower values of  $\alpha_{\text{vir}}$ ; as radius is correlated with mass we find that also more massive structures appear gravitationally bound. As velocity dispersion increases, so does  $\alpha_{\text{vir}}$ . However, in E when  $\sigma_v \geq 0.3 \text{ km s}^{-1}$  the relation appears to become double-sloped, as  $\alpha_{\text{vir}} \propto \sigma_v^{1.34}$  and another region where  $\alpha_{\text{vir}}$  is approximately constant.

Statistics of the subregions are listed in Table F.1, which lists the mean values over all structures associated with the subregion. Some subregions can be in multiple categories, for example the structures within the Spine in W are also part of the Body subregion. We show maps of estimated  $\alpha_{\text{vir}}$  for each individual structure in Figs. F.1–F.3 and of LSR velocity in Figs. F.4–F.6. In the  $\alpha_{\text{vir}}$  maps, those structures with  $\alpha_{\text{vir}} \leq 1$  (i.e. apparently gravitationally bound) are plotted in pink.

The compactness of the Front in E is seen in central velocity: the dispersion in  $v_{\text{cen}}$  in the Front is only  $0.2 \text{ km s}^{-1}$ , compared to  $1.6\text{--}1.8 \text{ km s}^{-1}$  in the Rim and Center. As the emission in the Rim comes from multiple structures along the line of sight (LOS), true column density and mass may be overestimated. However, as several dense cores and YSOs are located in the Rim, high-mass structures undoubtedly do exist. With the exception of a few substructures, the Head has a low  $\alpha_{\text{vir}}$  in both CO isotopologs, with the base structures showing  $\alpha_{\text{vir}} \sim 1\text{--}2$ . Both the Rim and Center show larger spread, with most (sub)structures having  $\alpha_{\text{vir}} \geq 5$  in  $^{13}\text{CO}$ . From virial analysis it appears that the Front could be in a state near gravitational instability; however CO has been shown to have low  $\alpha_{\text{vir}}$  even if structures are in fact dissipating (Szűcs et al. 2016). LSR velocity is constant in the Front but shows a v-shaped gradient in the Rim.

In both isotopologs of W, the base structure of the Body seems to be gravitationally bound with  $\alpha_{\text{vir}} \leq 1$ . The Back leg is less gravitationally bound than the front leg in  $^{12}\text{CO}$  ( $\alpha_{\text{vir}} = 2.5$  and 7.7 for the Front and Back legs, respectively). In addition, the Spine has low  $\alpha_{\text{vir}} \approx 1.6$ . The main Body and its subregions have little change in  $v_{\text{cen}} \sim 10 \text{ km s}^{-1}$ , with velocity decreasing toward the NE wings as well as toward the Front leg.

The Head in S is denser than the diffuse Legs. S has a high  $\alpha_{\text{vir}}$ , with most base-level structures showing  $\alpha_{\text{vir}} \geq 8$ , and in fact there seem to be no virially bound structures in S. The High-Velocity Cloud has a significantly higher central velocity of  $\sim 9.5 \text{ km s}^{-1}$ , com-

pared to around -4 to +4 km s<sup>-1</sup> in the rest of S. As it is not connected to the rest of the  $\lambda$  Orionis S cloud in PPV space, the High-Velocity Cloud may be a background structure unconnected with the field in physical space.

## 5. Discussion

### 5.1. Magnetic fields and formation of structures

In general, filaments are found to be parallel to the B-field at low densities, becoming perpendicular around  $N(\text{H}_2) \sim 10^{21} \text{ cm}^{-2}$  (Planck Collaboration et al. 2016). Filaments using low-density tracers ( $W(^{12}\text{CO})$ ,  $W(^{13}\text{CO})$ ) in the Vela C cloud have been observed to be parallel to the B-field, whereas filaments detected with high-density gas tracers are more likely to be perpendicular to the B-field (Fissel et al. 2019). Low-density  $^{12}\text{CO}$  filaments in Taurus are also preferentially aligned with the B-field (Goldsmith et al. 2008). However, there is large variation in relative orientation between the B-field and filaments (Pattle et al. 2023). For example, Zhao et al. (2025) also detect B-fields parallel to the entire body of the massive G37 filament regardless of local column density at a resolution of 2'. We do not recover the usual transition in column densities, likely due to the geometry of the region and the effect of feedback.

Confusion along the LOS can account for poor alignment between the B-field and filaments; certainly in the Rim in E, Wings in W, and Legs in S this is a concern. This same poor alignment of polarization angle is also detected in starlight polarization observations of Saha et al. (2022), who detect  $\Psi_B$  between 18° and 180° in the Front of E. There is no clear link between the detected small-scale filaments and the B-field; rather the turbulence is likely dominated by feedback. The main angle of the E cloud is parallel to the direction of radiation, probably carved out of the ISM by UV radiation and stellar winds. In W, the main structure of the cloud is parallel to the B-field, and perpendicular to the direction of radiation. The Meissa-facing edge of W is likely to have been formed through compression of gas by the expanding H II region. As the B-field in this region follows the rim of the  $\lambda$  Orionis ring, we expect that feedback dominates and the B-field lines are being dragged along with the gas. The formation of the Head, Front- and Back Legs in W are more uncertain. They could be similar structures to the Head in  $\lambda$  Orionis E, being carved out by radiation. R-band polarization observations by Neha et al. (2024) detect a more disorganized B-field in BRC-17 (the Head in W) when compared to BRC-18 (the Front in E). Within S, the B-field loops through the Head, however this structure seems to be part of a larger twisting of the B-field visible in the lower right corner of Fig. 5. In all, the strong UV radiation and the expanding H II region around Meissa likely have a stronger effect on the  $\lambda$  Orionis ring than B-fields.

Within the Pillars of Creation, Pattle et al. (2018) detect a B-field parallel to the long axis of their Pillar II, in contrast with the more perpendicular-aligned B-field in the ionized region (see Fig. 5 in Pattle et al. 2018). This type of organized B-field morphology is not detected at the *Planck* resolution in  $\lambda$  Orionis nor with starlight polarization by Saha et al. (2022). Whether a more complicated B-field morphology would be visible with higher-resolution polarization observations of the full fields is unknown. The B-field strength of 170 - 320  $\mu\text{G}$  estimated for the Pillars is up to an order of magnitude larger than that estimated for the irradiated rims of  $\lambda$  Orionis E and W ( $\sim 40 \mu\text{G}$  and  $\sim 28 \mu\text{G}$ , respectively) from R-band polarization by Neha et al. (2024).

### 5.2. $H_2$ and the effect of dust opacity

Dust temperatures and spectral index  $\beta$  estimated using MBB fitting are consistent with the values found in dense regions (Dupac et al. 2003; Juvela et al. 2015b,a; Zucker et al. 2018; Yi et al. 2018).  $H_2$  column densities of the order of  $10^{22} \text{ cm}^{-2}$  are also similar to those observed in nearby SF clouds with instruments such as *Herschel* (Zucker et al. 2018; Mannfors et al. 2021). CO column densities are consistent with the lower range of those calculated in the California MC, assuming a  $^{13}\text{CO}$ -to- $^{12}\text{CO}$  ratio of 1.69 (Pineda et al. 2010; Lewis et al. 2021).

It is well-known that dust opacity  $\kappa$  varies within the ISM (Planck Collaboration et al. 2014), and uncertainties in  $\kappa$  do propagate to other physical parameters such as temperature and column density. We have performed MBB fitting assuming  $\kappa_0 = 0.1$  or  $8.8 \times 10^{-3} \text{ cm}^2 \text{ g}^{-1}$  as well as  $\beta = [1.6, 1.8, 2.0, 2.2]$  or a free  $\beta$ . Mean temperature decreases by  $\sim 3.8 \text{ K}$  ( $3.4 \text{ K}$ ) for the front (back) regions when  $\beta$  is increased from 1.6 to 2.2, similar to the  $T$  and  $\beta$  anticorrelation which has been known to exist within the dense ISM (Dupac et al. 2003; Désert et al. 2008; Paradis et al. 2010; Juvela et al. 2015a). Column densities with the fitted  $\kappa_0$  are higher by up to 100%, but a higher  $\beta$  (lower  $T$ ) reduces this difference. The ratio  $N(\text{H}_2)_{\text{fit}}/N(\text{H}_2)_{\text{Beckwith}}$  at  $\beta = 1.6$  is 2.1 but when  $\beta = 2.2$  the two column densities are almost the same as  $N(\text{H}_2)_{\text{fit}}/N(\text{H}_2)_{\text{Beckwith}} = 1.1$ . If assuming the Beckwith et al. (1990)  $\kappa_0$ , our *Herschel* column densities would be of the order of  $1 \times 10^{21} \text{ cm}^{-2}$  leading to lower  $X_H(^{12}\text{CO}) \sim 2.2 \times 10^{20} \text{ cm}^{-2} \text{ km}^{-1} \text{ s K}^{-1}$  and higher abundances of  $\sim 4.7 \times 10^{-5}$ .

In Taurus, the normalized extinction PDFs show a Gaussian distribution with a tail at both high and low  $A_v$  (Pineda et al. 2010). While our data also show a low- $A_v$  tail, at the high end the PDF is well-fitted by a Gaussian. Kainulainen et al. (2009) have found that high  $A_v$  tails are only detected in regions of active SF, whereas quiescent MCs are better fitted by a log-normal. Though the  $\lambda$  Orionis ring cannot be called quiescent, it does not host much SF when compared to similar clouds (Yi et al. 2018).

### 5.3. CO

$N(^{12}\text{CO})$  values of  $10^{16}$ - $10^{18} \text{ cm}^{-2}$  have been observed in the Taurus MC (Pineda et al. 2010), around 30% of which are in the non-LTE state (their Mask 1). Roueff et al. (2021) estimated column densities  $N(^{12}\text{CO}) \sim 10^{16}$ - $10^{19} \text{ cm}^{-2}$  in Orion B. The values of CO column densities in  $\lambda$  Orionis are consistent with these values, assuming the majority of the total CO mass is in  $^{12}\text{CO}$ . For derivation of  $N(\text{CO})$  we combined LTE and non-LTE regions. At TRAO resolution 46% of  $\lambda$  Orionis E is in non-LTE conditions; in S at Planck resolution 37% of pixels with data cover non-LTE regions.

### 5.4. X-factors

Higher  $X$ -factor is expected in regions with a high UV field due to photodissociation of the CO molecule (Shetty et al. 2011). On the other hand, simulations have shown that  $X$ -factor decreases with increasing UV fields at low metallicities, as also  $H_2$  is suppressed by a strong UV field (Feldmann et al. 2012). In five Local Group galaxies, Leroy et al. (2011) also detect decreasing  $\alpha_{\text{CO}}$ , the CO-to- $H_2$  mass conversion factor, with increasing metallicity. This decrease from high to "normal"  $\alpha_{\text{CO}}$  occurs suddenly at metallicity  $Z \sim 0.25 Z_\odot$ .

Mean  $X_H$  in our fields is around the Galactic mean, but with a wide spread. As Figs. 14 and 17 show, the peak of the  $X_H$  his-

togram is around half of  $X_{\text{Gal}}$  but with a second peak at  $\sim 10X_{\text{Gal}}$ . We detect an increase in mean  $X(^{12}\text{CO})$  between the Front and Rim in E; in the Rim this value is  $\sim 1.9X_{\text{Gal}}$  and in the Front is is consistent with  $X_{\text{Gal}}$ . We do not however detect correlation between the distance to Meissa and the X-factor on a pixel-by-pixel basis in E.

As X-factor has been shown to depend on local volume density, variation in X can be used to differentiate between regions which appear to have high column density due to LOS overlap and those regions which are unified, dense regions (Shetty et al. 2011). This is detected in our data: mean  $N_{\mathcal{H}}$  in both the Rim and Front of E is around  $(2 - 3) \times 10^{21} \text{ cm}^{-2}$ . In contrast, both  $X(^{12}\text{CO})$  and  $X(^{13}\text{CO})$  are lower by around 30% in the Front which is a unified structure in PPV space. We further detect much lower variation in X-factor in the Front than the Rim ( $\sigma(X(^{12}\text{CO})) = (2.7 \text{ and } 4.9) \times 10^{20} \text{ cm}^{-2} \text{ km}^{-1} \text{ s K}^{-1}$  in the Front and Rim, respectively). Plots of  $N(\text{H}_2)$  against  $X(\text{CO})$  (Figs. E and 4.7, frames j-k) show increasing X-factor with higher column density. This is also seen in MBM12 in BFROST II, where even at *Herschel* resolution the transition toward molecular CO is unresolved.

Our data cover only the lower part of the  $A_v$  -  $X(\text{CO})$  histograms shown in Fig. 6 of Szűcs et al. (2016). Comparing their figure to the plots of E (Fig. 17),  $\lambda$  Orionis best fits those simulations with solar metallicity and dense regions, but with an intermediate-strength radiation field. At low metallicities  $X(^{12}\text{CO})$  is likely to be above  $X_{\text{Gal}}$ , unlike what we detect in  $\lambda$  Orionis. As the  $\lambda$  Orionis ring has been believed to contain supernova ejecta, we would expect higher metallicities in this region. The *Herschel* maps do not cover regions of low or intermediate extinction,  $A_v \leq 1 \text{ mag}$ . We detect a rapid decrease of  $X(\text{CO})$  in the translucent region  $A_v \approx 1 - 2 \text{ mag}$ , signaling the region in which carbon is converted from atomic form to molecular. At higher extinctions  $A_v \geq 2 \text{ mag}$ , CO again saturates leading to increased  $X(\text{CO})$ . We see this saturation point in  $X(^{12}\text{CO})$  at  $A_v \sim 2 - 3 \text{ mag}$  in the Rim but at slightly lower values of  $A_v \sim 1.5 - 2 \text{ mag}$  in the Front. Interestingly, we also detect saturation of  $X(^{13}\text{CO})$  in both the Front and Rim, beginning at  $A_v \sim 1 - 4 \text{ mag}$ .

### 5.5. Abundances

The abundances in both the  $\lambda$  Orionis ring (at *Herschel* resolution) and in MBM12 are low compared to the canonical high-extinction fractional abundance value of  $\sim 10^{-4}$  found in regions such as Taurus (Pineda et al. 2008; Herbst & van Dishoeck 2009; Pineda et al. 2010), and even compared to the nearby region Orion B (Roueff et al. 2021). Even lower abundances around  $10^{-6}$  have been observed in more diffuse regions in Taurus (e.g. Mask 0 in Pineda et al. 2010). In dense (but not depleted) regions such as in the Head of E the abundance reaches values close to the canonical value. Outside of self-shielded dense regions the  $\lambda$  Orionis clouds are exposed to high UV radiation which dissociates the CO molecules, leading to a naturally lower abundance.

Calculation of column densities obviously affects the scale of the abundance. As we showed, the assumption of the commonly-used  $\kappa_0 = 0.1 \text{ cm}^{-2} \text{ g}^{-1}$  at 1000 GHz would increase abundance by around 25%. Furthermore, the usage of LTE and non-LTE regions will change derived abundances: calculating this value in only  $^{13}\text{CO}$ -bright regions results in an increase of mean abundance of  $\sim 60\%$ . CO column densities in e.g. Pineda et al. (2010) are estimated using a constant  $^{12}\text{CO}$ -to- $^{13}\text{CO}$  ratio, whereas we use the variable ratios estimated by Szűcs et al. (2014). That both MBM12 and  $\lambda$  Orionis show this trend of relatively low  $[\text{CO}/\text{H}_2]$

suggests that this deviance from the literature is due to data analysis methods.

### 5.6. Depleted cores within $\lambda$ Orionis E

In both X-factor and abundance, we notice depletion toward the densest cores in the Front and Rim, as well as in the dense filamentary ridge in the Front. This depletion is clear also in Fig. 17; X-factor increases sharply above  $A_v \geq 3 - 5$  in both isotopologs. We used AStereoDendro to extract the depleted cores in the  $X_{\mathcal{H}}(^{12}\text{CO})$  map.  $X_{\mathcal{H}}$  maps as opposed to abundance maps are used because the depleted cores are minima in the abundance maps and thus will not be detected as structures by AStereoDendro. We detected two structures which correspond to PGCC G196.92-10.37 (marked with (a) in Fig. 2) which is a core containing a Class 0 protostar (Yi et al. 2018). From SCUBA-2 data, they estimated that the core has a column density of  $(18.2 \pm 1.3) \times 10^{22} \text{ cm}^{-2}$  and a mass of  $\sim 5.4 \pm 0.3 M_{\odot}$ .

The two structures we detected have radii of 0.06 and 0.07 pc, mean  $X_{\mathcal{H}}(^{12}\text{CO})$  of  $\sim 2.5 \pm 0.8 X_{\text{Gal}}$  and mean  $[\text{CO}/\text{H}_2] \approx 0.65 \pm 0.15 \times 10^{-4}$ . These structures have mean  $N_{\mathcal{H}} \approx 18 \pm 10 \times 10^{21} \text{ cm}^{-2}$ . We further detected a potential depleted core in the Rim of size 0.05 pc, with mean  $X_{\mathcal{H}}(^{12}\text{CO})$  of  $\sim 2.6 \pm 0.8 X_{\text{Gal}}$  and mean  $[\text{CO}/\text{H}_2] \approx 0.31 \pm 0.10$ .

### 5.7. Gravitational stability

In most structures  $\alpha_{\text{vir}} \geq 1$ , suggesting that most of the  $\lambda$  Orionis region is not collapsing under gravity. Given the high energy environment and the possible blowing away of the clouds due to UV radiation and stellar winds detected by Saha et al. (2022) in E, it is likely that the  $\lambda$  Orionis ring is being dispersed by stellar feedback. Furthermore, we do not account for radiative pressure from the UV radiation which could compress the  $\lambda$  Orionis clouds, enabling gravitational collapse. Certainly the presence of two protostellar clumps and the strong CO depletion suggest triggered SF in the Meissa-facing rim of the  $\lambda$  Orionis cloud.

It appears that larger structures are more gravitationally unstable in our data. A similar relation within dense cores has been detected in other clouds, including California, the Pipe nebula, and Orion A (Lada et al. 2008; Kirk et al. 2017; Lewis et al. 2021). A relation between  $\alpha_{\text{vir}}$  and mass is expected in virialized clouds  $1 < \alpha_{\text{vir}} < 2$ , but only if external pressure is taken into account (Bertoldi & McKee 1992).

We estimated the virial mass using the structure mass and internal velocity dispersion and assumed spherical symmetry (Eq. B.3). Clump masses were estimated using the mean X-factor of the cloud (Eq. B.2). Virial analysis however neglects outside turbulence, likely to be quite high at the edge of a H II region, as well as magnetic support (or dispersion). While the assumption of spherical symmetry can work in dense cores, it is a poor assumption in larger-scale structures and filaments which will collapse along their shortest axis.  $X_{\mathcal{H}}$  also changes by a factor of five in E; the mean  $X_{\mathcal{H}}(^{12}\text{CO})$  is likely to be a poor assumption within the dense depleted cores. Simulations by Szűcs et al. (2016) show that virial parameters estimated from CO-bright gas are lower than the true value, and this difference is especially large in regions with high  $\alpha_{\text{vir}}$ . Additional sources contributing to artificially low  $\alpha_{\text{vir}}$  include incomplete removal of background or foreground emission, lack of observational resolution, and bulk kinetic energies (Singh et al. 2021). In all, we caution against too literal an interpretation of  $\alpha_{\text{vir}}$ . Without a full understanding of the three-dimensional structure of the region, high-resolution

B-field values, and an estimate of the external pressure, virial analysis can give only a rough idea of the gravitational stability of these regions.

### 5.8. Comparison with MBM12

MBM12 is a nearby, quiescent cloud which was also observed as part of the B-FROST survey (Vorster et al., *in prep.*). It has been analyzed with many of the same methods as were used in this paper, and as a quiescent cloud is an excellent comparison to the energetic  $\lambda$  Orionis ring. Though H<sub>2</sub> column densities are consistent, the  $X_H$  PDF of  $\lambda$  Orionis has a sharper peak than that of MBM12. Mean  $N(\text{CO})$  is of the same order in MBM12 and  $\lambda$  Orionis, though reaching somewhat higher values in the densest filaments of  $\lambda$  Orionis. Due to the smaller distance of MBM12 (252 pc), the physical resolution of the MBM12 observations is just under 50% smaller than of  $\lambda$  Orionis: at the TRAO resolution we can detect structures of size 0.05 pc, compared to  $\sim 0.09$  pc in  $\lambda$  Orionis. Despite this, we do not detect  $^{13}\text{CO}$  depletion in the MBM12 cloud.

Abundances are of the same order in both MBM12 and E, as are X-factors. Comparison between Fig. 4.7 and the corresponding figure for MBM12 shows a few clear differences. In both E and MBM12,  $T_{\text{ex}}$  shows more scatter at low temperatures, however  $\lambda$  Orionis reaches higher  $T_{\text{ex}}$  than MBM12 (a maximum around 30 K for E and around 17 K for MBM12). In this paper we detect  $^{13}\text{CO}$  saturation when plotting  $N(\text{H}_2)$  against  $W(^{13}\text{CO})$  (frame f) at around  $W(^{13}\text{CO}) \sim 10 \text{ K km s}^{-1}$ ; no saturation is detected in MBM12. The comparison between  $N(\text{CO})$  and X-factors (frames g, h) are similar in  $^{13}\text{CO}$ . In  $^{12}\text{CO}$  in MBM12, the cutoff point is clear and after this point,  $X(^{12}\text{CO})$  stays approximately constant. In E, the pixels with high  $T_{\text{ex}}$  have constant  $X(^{12}\text{CO})$  as in MBM12 but there are many pixels in which  $X(^{12}\text{CO})$  saturates very quickly. The plots between abundance and  $X(^{12}\text{CO})$  are similar, but in MBM12 we did not detect any correlation between [CO/H<sub>2</sub>] and  $X(^{13}\text{CO})$ . In contrast, the [CO/H<sub>2</sub>] against  $X(^{13}\text{CO})$  plot in E has a strong decrease with increasing abundance, similar in shape to the plot of  $^{12}\text{CO}$ .

## 6. Summary

The BFROST survey provides a varied sample of large-scale spectral line maps of the dense ISM, and is thus ideal to compare the properties of the gas and dust in differing Galactic environments. BFROST-I presented the survey overview, and in this paper we present the result for three fields in the  $\lambda$  Orionis region. The  $\lambda$  Orionis ring is an excellent example of a molecular ring experiencing strong UV radiation and the perfect environment to understand the effect of feedback on molecular gas. Other B-FROST papers will compare this region to more quiescent regions such as MBM12 (Vorster et al., *in prep.*) as well as high-mass regions such as Monoceros OB1 (Montillaud et al., *in prep.*).

In our analysis of  $\lambda$  Orionis we find

- Using *Herschel* SPIRE data, we estimate mean  $N(\text{H}_2) \approx 2 \times 10^{21} \text{ cm}^{-2}$  and mean CO column densities of the order of  $10^{17} \text{ cm}^{-2}$ . Mean  $X(^{12}\text{CO})$  is around  $3.5 \times 10^{20} \text{ cm}^{-2} (\text{km s}^{-1} \text{ K})^{-1}$  and  $X(^{13}\text{CO})$  is around  $15 \times 10^{20} \text{ cm}^{-2} (\text{km s}^{-1} \text{ K})^{-1}$ . At the Planck resolution, column densities can be an order of magnitude lower due to smearing of structures with the larger *Planck* beam and the higher dust temperatures used by *Planck*. This naturally leads to lower estimated X-factors

and higher abundances, and thus X-factors estimated with *Planck* data are a factor of ten lower.

- CO-to-H<sub>2</sub> abundances are a few times  $10^{-5}$  using  $N(\text{H}_2)$  estimated from *Herschel* data. Fitting a linear relation between  $N_H$  and  $N(\text{CO})$  results in

$$\begin{aligned} N(\text{CO})_{\text{all}} &\propto (0.4 \times 10^{-4})N(\text{H}_2), \\ N(\text{CO})_{\text{Rim}} &\propto (0.3 \times 10^{-4})N(\text{H}_2), \\ N(\text{CO})_{\text{Front}} &\propto (0.6 \times 10^{-4})N(\text{H}_2), \end{aligned}$$

for the whole field, Rim, and Front subregions, respectively.

- We detect depletion in dense cores using both abundance and X-factor in both  $^{12}\text{CO}$  and  $^{13}\text{CO}$  in  $\lambda$  Orionis E.
- Virial parameter  $\alpha_{\text{vir}}$  is high in  $\lambda$  Orionis, suggesting clouds which are dispersing. It is likely that the strong feedback from Meissa is dissipating the  $\lambda$  Orionis ring. The presence of dense cores and ancillary YSO data in the Meissa-facing regions of  $\lambda$  Orionis suggest compression of the gas by the expanding H II region. It is likely that many of the dense cores are pressure-bound; however we note the limitations of the virial parameter in estimating cloud stability.
- We detect polarization fraction  $p$  of 4-7% across the  $\lambda$  Orionis clouds with lower  $p$  being found in regions with higher  $N(\text{H}_2)$ .
- Feedback has a stronger effect on the  $\lambda$  Orionis region than B-fields. Detected filaments in these fields are slightly more likely to be perpendicular to the magnetic field at low  $W(^{12}\text{CO})$  and parallel at high  $W(^{12}\text{CO})$ , in contrast to the usual trend of increased perpendicular alignment at high column densities. The correlation between filament and B-field position angle is weak, however. Instead, e.g. the long axis of the  $\lambda$  Orionis E cloud is aligned with the direction of radiation from Meissa.

**Acknowledgements.** EM is funded by a grant from the Viljo, Yrjö, and Kalle Väisälä Foundation of the Finnish Academy of Sciences and Letters. DA acknowledges the Faculty Development Competitive Research Grant Program of Nazarbayev University No. 201223FD8821. VMP gratefully acknowledges financial support from the European Research Council via the ERC Synergy Grant "ECOGAL" (project ID 855130). MJ and JV acknowledge support from the Academy of Finland grant No 348342. The authors gratefully acknowledge the support of the TRAO observatory staff during observations. This research has made use of "Aladin sky atlas" developed at CDS, Strasbourg Observatory, France. This research made use of astrodendro, a Python package to compute dendograms of Astronomical data (<http://www.dendrograms.org/>)

## References

- Acharyya, K., Fuchs, G. W., Fraser, H. J., van Dishoeck, E. F., & Linnartz, H. 2007, A&A, 466, 1005
- Alina, D., Montillaud, J., Hu, Y., et al. 2022, A&A, 658, A90
- Barnard, E. E. 1919, ApJ, 49, 1
- Barnard, E. E. 1927, Catalogue of 349 dark objects in the sky
- Beckwith, S. V. W., Sargent, A. I., Chini, R. S., & Guesten, R. 1990, AJ, 99, 924
- Bergin, E. A., Langer, W. D., & Goldsmith, P. F. 1995, ApJ, 441, 222
- Bertoldi, F. & McKee, C. F. 1992, ApJ, 395, 140
- Bohlin, R. C., Savage, B. D., & Drake, J. F. 1978, ApJ, 224, 132
- Bolatto, A. D., Wolfire, M., & Leroy, A. K. 2013, ARA&A, 51, 207
- Carrière, J. S., Ferrière, K., Ristorcelli, I., & Montier, L. 2022a, A&A, 668, A42
- Carrière, J. S., Montier, L., Ferrière, K., & Ristorcelli, I. 2022b, A&A, 668, A41
- Chuss, D. T., Hensley, B. S., Kogut, A. J., et al. 2022, ApJ, 940, 59
- Cutri, R. M., Skrutskie, M. F., van Dyk, S., et al. 2003, VizieR Online Data Catalog, II/246
- de Almeida, E. S. G., Marcolino, W. L. F., Bouret, J. C., & Pereira, C. B. 2019, A&A, 628, A36
- Désert, F. X., Macías-Pérez, J. F., Mayet, F., et al. 2008, A&A, 481, 411
- Dupac, X., Bernard, J. P., Boudet, N., et al. 2003, A&A, 404, L11
- Feldmann, R., Gnedin, N. Y., & Kravtsov, A. V. 2012, ApJ, 747, 124
- Ferrière, K. M. 2001, Reviews of Modern Physics, 73, 1031

- Fissel, L. M., Ade, P. A. R., Angilè, F. E., et al. 2019, *ApJ*, 878, 110  
 Goldsmith, P. F., Heyer, M., Narayanan, G., et al. 2008, *ApJ*, 680, 428  
 Gould, R. J. & Salpeter, E. E. 1963, *ApJ*, 138, 393  
 Hamaker, J. P. & Bregman, J. D. 1996, *A&AS*, 117, 161  
 Herbst, E. & van Dishoeck, E. F. 2009, *ARA&A*, 47, 427  
 Heyer, M. & Dame, T. M. 2015, *ARA&A*, 53, 583  
 HI4PI Collaboration, Ben Bekhti, N., Flöer, L., et al. 2016, *A&A*, 594, A116  
 Hollenbach, D. & Salpeter, E. E. 1971, *ApJ*, 163, 155  
 Hollenbach, D. J., Werner, M. W., & Salpeter, E. E. 1971, *ApJ*, 163, 165  
 Jeong, I.-G., Kang, H., Jung, J., et al. 2019, *Journal of Korean Astronomical Society*, 52, 227  
 Juvela, M., Demyk, K., Doi, Y., et al. 2015a, *A&A*, 584, A94  
 Juvela, M., Ristorcelli, I., Marshall, D. J., et al. 2015b, *A&A*, 584, A93  
 Kainulainen, J., Beuther, H., Henning, T., & Plume, R. 2009, *A&A*, 508, L35  
 Kirk, H., Friesen, R. K., Pineda, J. E., et al. 2017, *ApJ*, 846, 144  
 Lada, C. J., Muench, A. A., Rathborne, J., Alves, J. F., & Lombardi, M. 2008, *ApJ*, 672, 410  
 Lang, W. J., Masheder, M. R. W., Dame, T. M., & Thaddeus, P. 2000, *A&A*, 357, 1001  
 Larson, R. B. 1981, *MNRAS*, 194, 809  
 Leroy, A. K., Bolatto, A., Gordon, K., et al. 2011, *ApJ*, 737, 12  
 Lewis, J. A., Lada, C. J., Bieging, J., et al. 2021, *ApJ*, 908, 76  
 Lewis, J. A., Lada, C. J., & Dame, T. M. 2022, *ApJ*, 931, 9  
 Lombardi, M. 2009, *A&A*, 493, 735  
 Lombardi, M. & Alves, J. 2001, *A&A*, 377, 1023  
 Lombardi, M., Bouy, H., Alves, J., & Lada, C. J. 2014, *A&A*, 566, A45  
 Maddalena, R. J. & Morris, M. 1987, *ApJ*, 323, 179  
 Mangum, J. G. & Shirley, Y. L. 2015, *PASP*, 127, 266  
 Mannfors, E., Juvela, M., Bronfman, L., et al. 2021, *A&A*, 654, A123  
 Marton, G., Ábrahám, P., Szegedi-Elek, E., et al. 2019, *MNRAS*, 487, 2522  
 McKee, C. F. & Krumholz, M. R. 2010, *ApJ*, 709, 308  
 Neha, S., Soam, A., & Maheswar, G. 2024, *A&A*, 689, A225  
 Ostriker, E. C., Stone, J. M., & Gammie, C. F. 2001, *ApJ*, 546, 980  
 Paradis, D., Veneziani, M., Noriega-Crespo, A., et al. 2010, *A&A*, 520, L8  
 Passot, T. & Vázquez-Semadeni, E. 1998, *Phys. Rev. E*, 58, 4501  
 Pattle, K., Fissel, L., Tahani, M., Liu, T., & Ntormousi, E. 2023, in *Astronomical Society of the Pacific Conference Series*, Vol. 534, *Protostars and Planets VII*, ed. S. Inutsuka, Y. Aikawa, T. Muto, K. Tomida, & M. Tamura, 193  
 Pattle, K., Ward-Thompson, D., Hasegawa, T., et al. 2018, *ApJ*, 860, L6  
 Pineda, J. E., Caselli, P., & Goodman, A. A. 2008, *ApJ*, 679, 481  
 Pineda, J. L., Goldsmith, P. F., Chapman, N., et al. 2010, *ApJ*, 721, 686  
 Planck Collaboration, Abergel, A., Ade, P. A. R., et al. 2014, *A&A*, 566, A55  
 Planck Collaboration, Ade, P. A. R., Aghanim, N., andAlves, M. I. R., et al. 2016, *A&A*, 586, A138  
 Planck Collaboration, Ade, P. A. R., Aghanim, N., et al. 2015, *A&A*, 576, A104  
 Ripple, F., Heyer, M. H., Gutermuth, R., Snell, R. L., & Brunt, C. M. 2013, *MNRAS*, 431, 1296  
 Robitaille, T., Rice, T., Beaumont, C., et al. 2019  
 Rosolowsky, E. W., Pineda, J. E., Kauffmann, J., & Goodman, A. A. 2008, *ApJ*, 679, 1338  
 Roueff, A., Gerin, M., Gratier, P., et al. 2021, *A&A*, 645, A26  
 Sadavoy, S. I., di Francesco, J., André, P., et al. 2012, *A&A*, 540, A10  
 Saha, P., Gopinathan, M., Ojha, D. K., & Neha, S. 2022, *MNRAS*, 510, 2644  
 Savage, B. D. & Mathis, J. S. 1979, *ARA&A*, 17, 73  
 Scalo, J., Vázquez-Semadeni, E., Chappell, D., & Passot, T. 1998, *ApJ*, 504, 835  
 Shetty, R., Glover, S. C., Dullemond, C. P., & Klessen, R. S. 2011, *MNRAS*, 412, 1686  
 Singh, A., Matzner, C. D., Friesen, R. K., et al. 2021, *ApJ*, 922, 87  
 Soler, J. D., Hennebelle, P., Martin, P. G., et al. 2013, *ApJ*, 774, 128  
 Sternberg, A., Le Petit, F., Roueff, E., & Le Bourlot, J. 2014, *ApJ*, 790, 10  
 Sugitani, K., Fukui, Y., & Ogura, K. 1991, *ApJS*, 77, 59  
 Szűcs, L., Glover, S. C. O., & Klessen, R. S. 2014, *MNRAS*, 445, 4055  
 Szűcs, L., Glover, S. C. O., & Klessen, R. S. 2016, *MNRAS*, 460, 82  
 Tassis, K., Christie, D. A., Urban, A., et al. 2010, *MNRAS*, 408, 1089  
 van der Tak, F. F. S., Black, J. H., Schöier, F. L., Jansen, D. J., & van Dishoeck, E. F. 2007, *A&A*, 468, 627  
 Vázquez-Semadeni, E. & García, N. 2001, *ApJ*, 557, 727  
 Visser, R., van Dishoeck, E. F., & Black, J. H. 2009, *A&A*, 503, 323  
 Yi, H.-W., Lee, J.-E., Liu, T., et al. 2018, *ApJS*, 236, 51  
 Zhao, M., Tang, X., Qiu, K., He, Y., & Li, D. 2025, *A&A*, 696, A178  
 Zucker, C., Battersby, C., & Goodman, A. 2018, *ApJ*, 864, 153  
 Zucker, C., Speagle, J. S., Schlafly, E. F., et al. 2019, *ApJ*, 879, 125

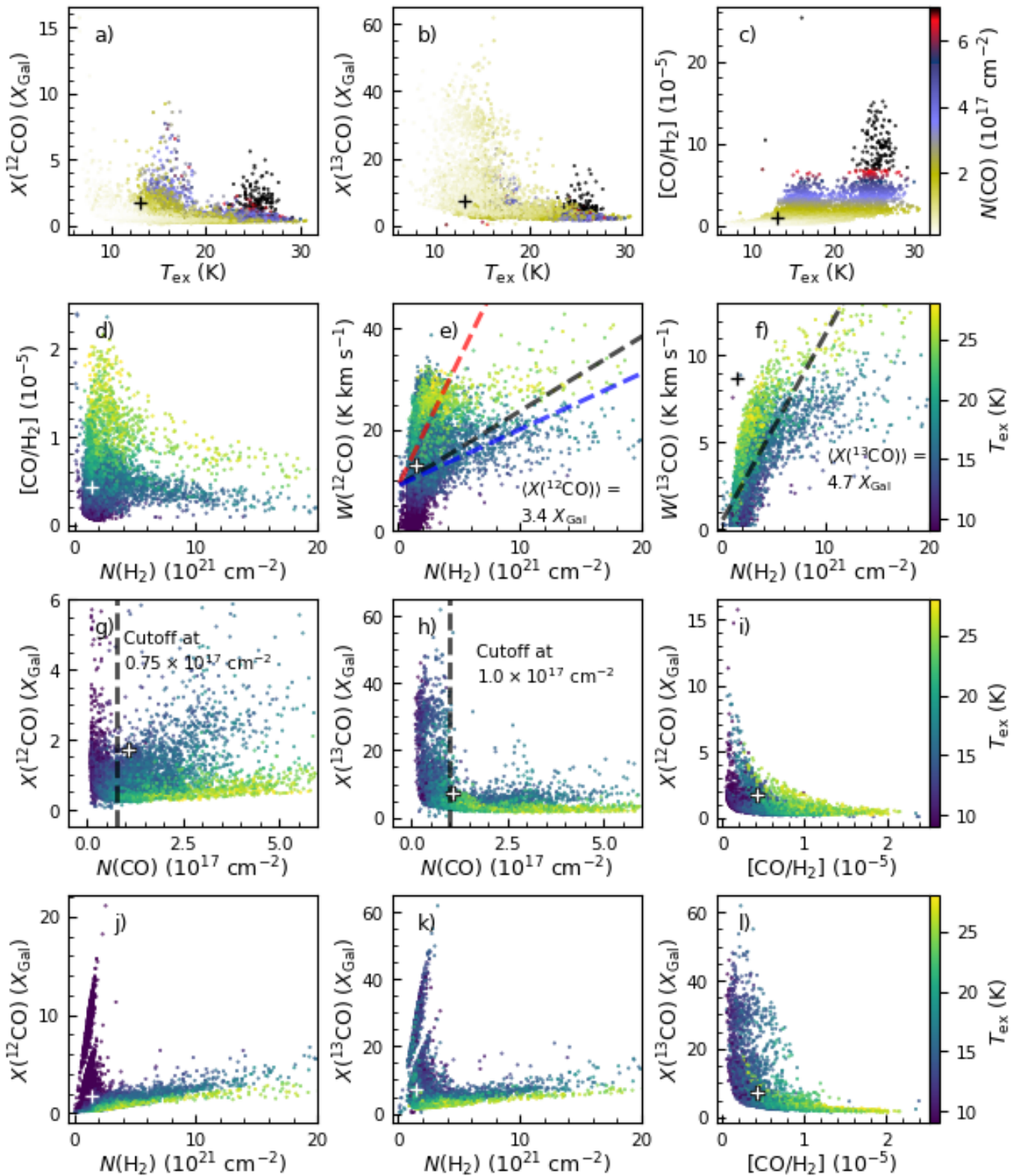


**Fig. 16.** Comparison of H<sub>2</sub> and CO properties in the  $\lambda$  Orionis E field at the TRAO resolution. The red and blue dashed lines in panel e correspond to  $X(^{12}\text{CO})$  of  $1 X_{\text{Gal}}$  and  $4.5 X_{\text{Gal}}$ , respectively. The white or black plus sign in each frame marks the mean value of each quantity.

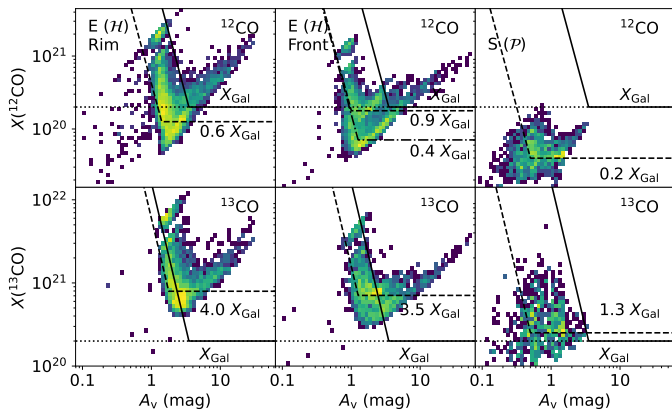


**Fig. 17.** Extinction  $A_v = N(H_2) \times 10^{-21}$  (Bohlin et al. 1978; Sadavoy et al. 2012) plotted against  $X(\text{CO})$  for  $^{12}\text{CO}$  (top) and  $^{13}\text{CO}$  (bottom) for the two *Herschel* fields in E and for  $S_P$ . The solid line shows the fit of Eq. 9, the dotted line to one based on the turning point in  $A_v$  and the mode of the histogram of  $X(\text{CO})$ . As in Fig. 6 of Szűcs et al. (2016).

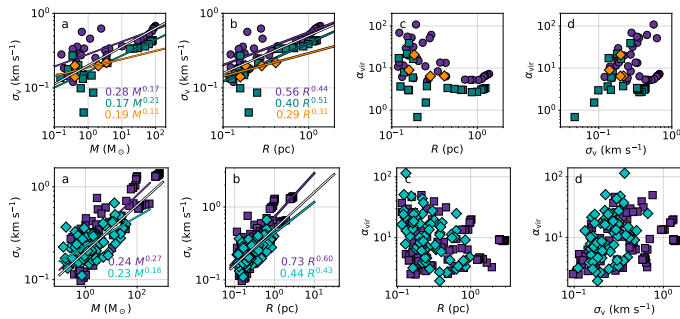


**Fig. 18.** Scale dependence of dendrogram substructures in E (top) and S (bottom) in  $^{13}\text{CO}$ . Powerlaw fits to some quantities are shown for each subregion. The Larson relations ( $\sigma \propto M^{0.25}$ ;  $\sigma \propto R^{0.5}$ , Larson (1981)) are shown on frames a and b in black-white solid lines. The colors and symbols indicate the subregions: Center (yellow diamonds), Rim (purple circles), and Front (teal squares) in E and Head (purple squares) and Legs (teal diamonds) in S.

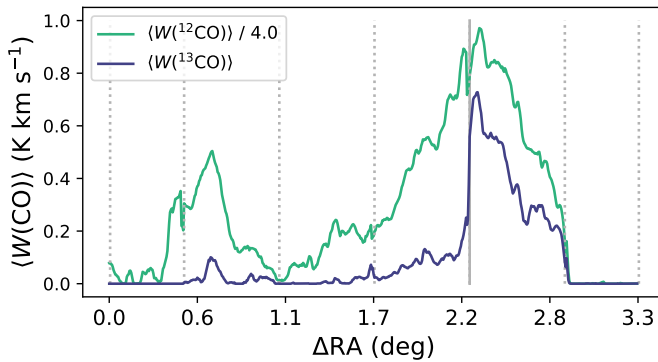


**Fig. A.1.** Mean line area in the  $^{12}\text{CO}$  and  $^{13}\text{CO}$  zeroth-moment maps of W, averaged along the y- (declination-) axis. The  $^{12}\text{CO}$  signal has been divided by four for viewing. The gray dotted vertical lines show the positions of the differing scans, the solid gray line shows the scan along which the jump in response is visible.

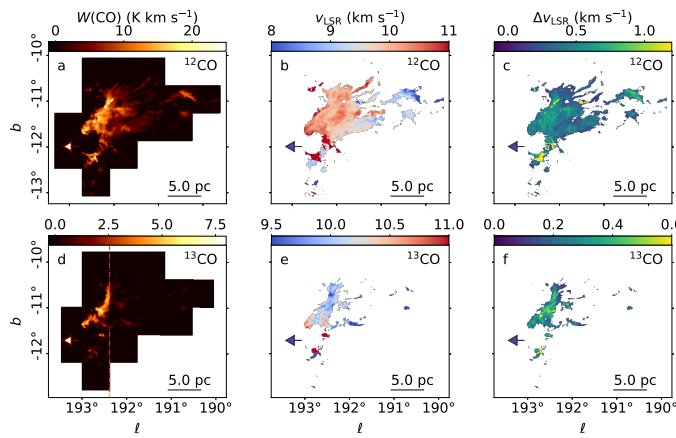


**Fig. A.2.** Zeroth-, first- and second-moment maps for  $\lambda$  Orionis W. The moment maps for the other fields are presented in BFROST-I. The orange line in the  $^{13}\text{CO}$  zeroth-moment map shows the break in signal level. The arrow points toward Meissa.

## Appendix A: $\lambda$ Orionis West

Due to errors in baselines, which we were not able to fix in data reduction, we limit analysis of  $\lambda$  Orionis W to only the region east of the orange line in Fig. A.2, d. The mean zeroth-moment signals, averaged along the scan direction, in W are shown in Fig. A.1; a steep increase in signal is visible at  $\Delta\text{RA} \approx 2.2^\circ$ . This sharp break in  $^{13}\text{CO}$  is in contrast to the signal in  $^{12}\text{CO}$  and is also visible in the zeroth-moment map (Fig. A.2, d). As the moment maps of W are not shown in BFROST-I, we present them here.

## Appendix B: Calculation of dendograms

Input parameters for AstroDendro are listed in Table B.1. The minimum value parameter is calculated as  $4\sigma$  over the entire datacube.

Dendrogram structures can be trunks, branches, or leaves. A trunk is a base-level structure, and a leaf is a top-level structure with no substructure. A branch is a structure within a trunk, which has further substructures. The substructures within a dendrogram region are known as descendants, direct descendants are also called children. The level of a dendrogram is calculated

**Table B.1.** Input parameters for AstroDendro

Parameter	Value ( $^{12}\text{CO}$ )	Value ( $^{13}\text{CO}$ )
min_npix	54	54
min_delt	0	0
min_value (E)	1.167	0.498
min_value (W)	1.146	0.487
min_value (S)	1.192	0.493

by AstroDendro. For each dendrogram branch, we calculate 14 parameters.

–  $\sum(T_{\text{mb2}})$  [K]  
The sum of all the pixels included in the structure within the entire datacube.

–  $A_{\text{exact}}$   
The exact area of a structure in arcmin<sup>2</sup>.

–  $v_{\text{cen}}$  [km s<sup>-1</sup>]  
The central velocity, calculated by

$$v_{\text{cen}} = \frac{\sum_{v=-40}^{v=40} (v_i \cdot T_{\text{struct},i})}{\sum(T_{\text{mb2}})}, \quad (\text{B.1})$$

where each frame  $i$  of the datacube  $T_{\text{struct},i}$  (including only those pixels which are included in the structure) is multiplied by its velocity  $v_i$ , and divided by  $\sum(T_{\text{mb2}})$ .

–  $\sigma_v$  [km s<sup>-1</sup>]  
The velocity dispersion, calculated using the array of velocities  $V$

$$\Delta v = (V - v_{\text{cen}})^2$$

$$\sigma_v = \frac{\sum_{v=-40}^{v=40} (T_{\text{struct},i} \times \Delta v_i)}{\sum(T_{\text{mb2}})}$$

–  $M_{\text{cl}}$  [ $M_\odot$ ]  
The mass of the structure, calculated as

$$M_{\text{cl}} = A_{\text{exact}} \cdot d^2 \cdot \mu_H m_H \cdot X \cdot \delta V \quad (\text{B.2})$$

where  $d$  is the distance to  $\lambda$  Orionis,  $X$  is the X-factor,  $\mu_H = 1.4$  is the mean molecular mass per hydrogen atom,  $m_H$  the mass of a Hydrogen atom, and  $\delta V = 0.2 \text{ km s}^{-1}$  is the velocity resolution of these observations.

–  $dM_{\text{cl}}$  [ $M_\odot$ ]  
The uncertainty of  $M_{\text{cl}}$ .

–  $\alpha_{\text{vir}}$   
The virial parameter of the structure. The estimated radius of the structure  $R$  is calculated assuming a circular clump with area  $A = A_{\text{exact}} = \pi R^2$ .

$$\alpha_{\text{vir}} = \frac{5\sigma_v^2 R}{G M_{\text{cl}}}, \quad (\text{B.3})$$

where G is the gravitational constant.

–  $d\alpha_{\text{vir}}$   
The uncertainty on  $\alpha_{\text{vir}}$ .

## Appendix C: Results of FilDreams analysis

The results of the FilDreams and HRO analysis are shown in Figs. C.1-C.3 for the three fields. For this analysis we have used *Planck* polarization data and  $W(^{12}\text{CO})$ .

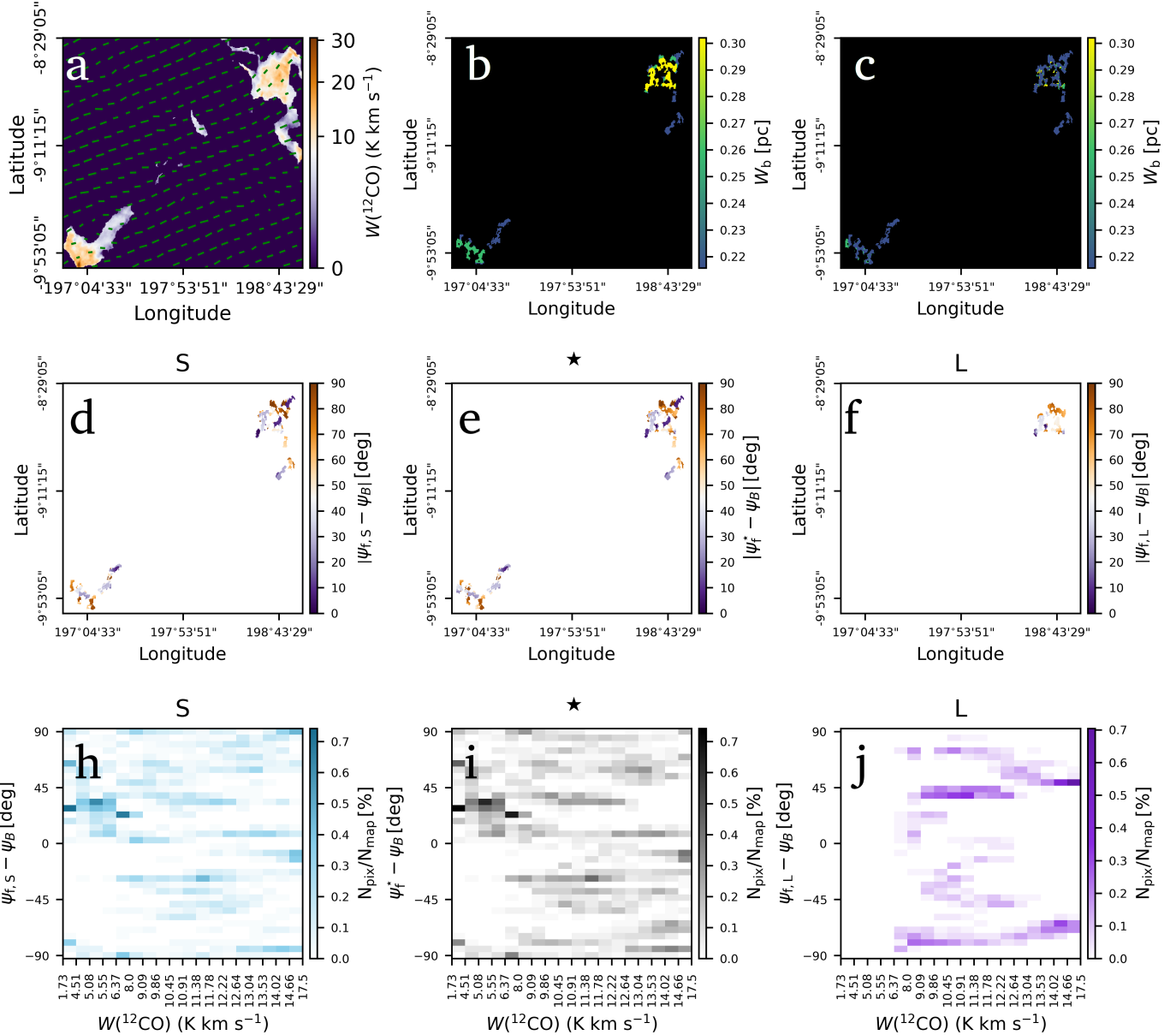


**Fig. C.1.** Results of the FilDReaMS analysis on  $\lambda$  Orionis E. Meissa is located in the direction of the bottom left corner of this image. (a) The B-field extracted from *Planck* polarization data. The length of each vector is proportional to the polarization fraction. The background image shows  $W(^{12}\text{CO})$ . (b) Map of the largest filament width  $W_b$  associated with each pixel (c) Map of the smallest filament width  $W_b$  associated with each pixel (d-f) Maps of filaments and their orientation relative to the B-field (d) at small scales (e) at all scales (f) at the largest scales. (h-j) The HROs as a function of  $W(^{12}\text{CO})$  (h) at small scales (i) at all scales (j) at the largest scales.

## Appendix D: Column density maps

We show column densities of the fields in Fig. D.1. Frames a-e show  $N(\text{H}_2)$ , frames f-h show  $N(\text{CO})$ , and frames i-l show  $W(\text{CO})$ .

## Appendix F: Dendrogram results

### F.1. Dendrogram outputs

We present maps and trees of  $\alpha_{\text{vir}}$  and  $V_{\text{LSR}}$  for each observation in Sections F.1.1-F.1.2. Subregion statistics are shown in Table F.1.

### F.1.1. Virial alpha

The following images show virial alpha  $\alpha_{\text{vir}}$  for the fields. We define the limit for gravitational boundedness as  $\alpha_{\text{vir}} \leq 1$  and plot these substructures with pink.

## Appendix E: Scatterplots of parameters

We compare parameters for S at the *Planck* resolution in Fig. E. The plot for E at the *Herschel* resolution is shown in the main text.

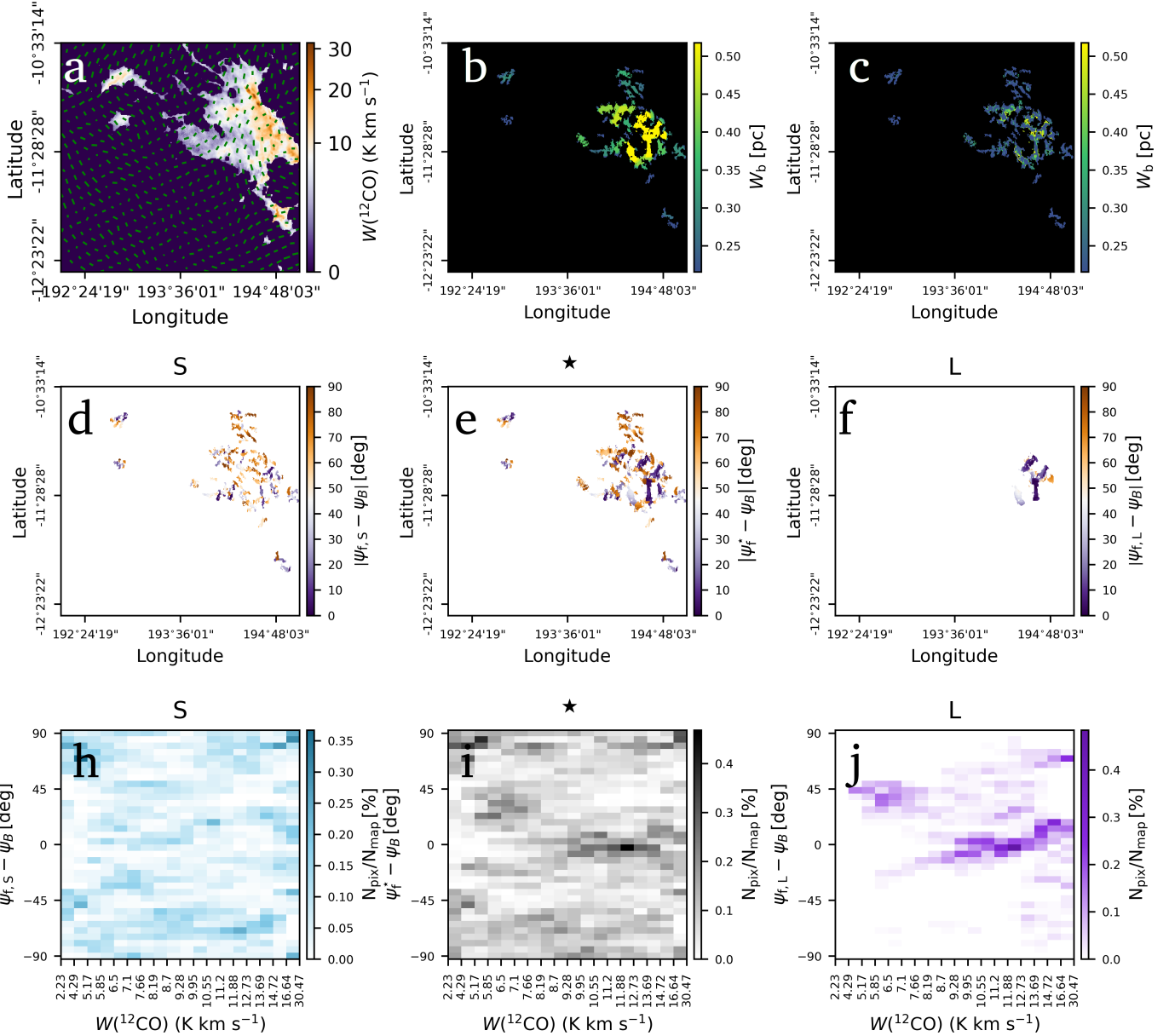


**Fig. C.2.** Same as Fig. C.1 for W. Meissa is located to the right of this image.

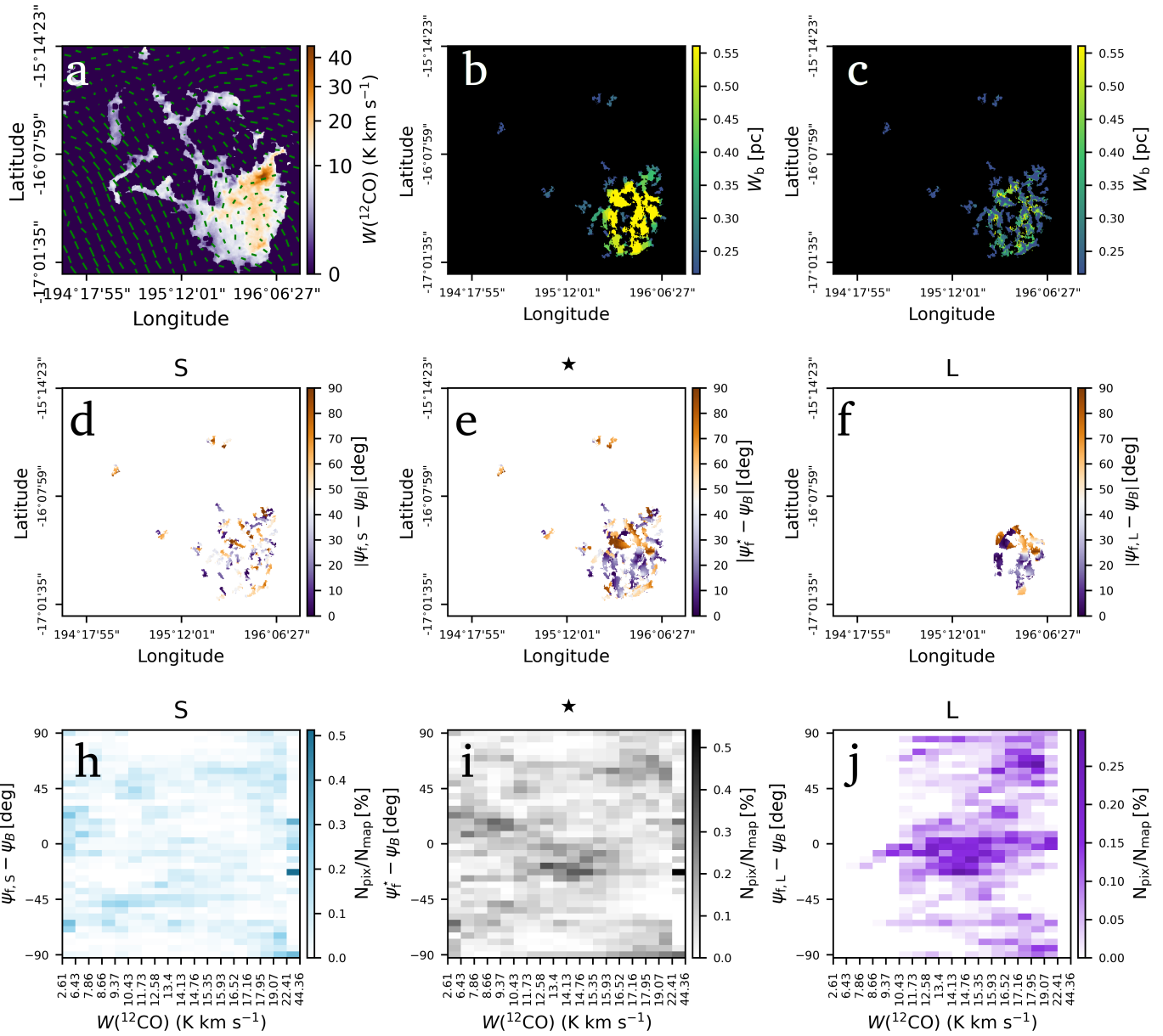
### F1.2. VLSR

The following images show central velocity  $v_{\text{cen}}$  for both isotopologs of each cloud.

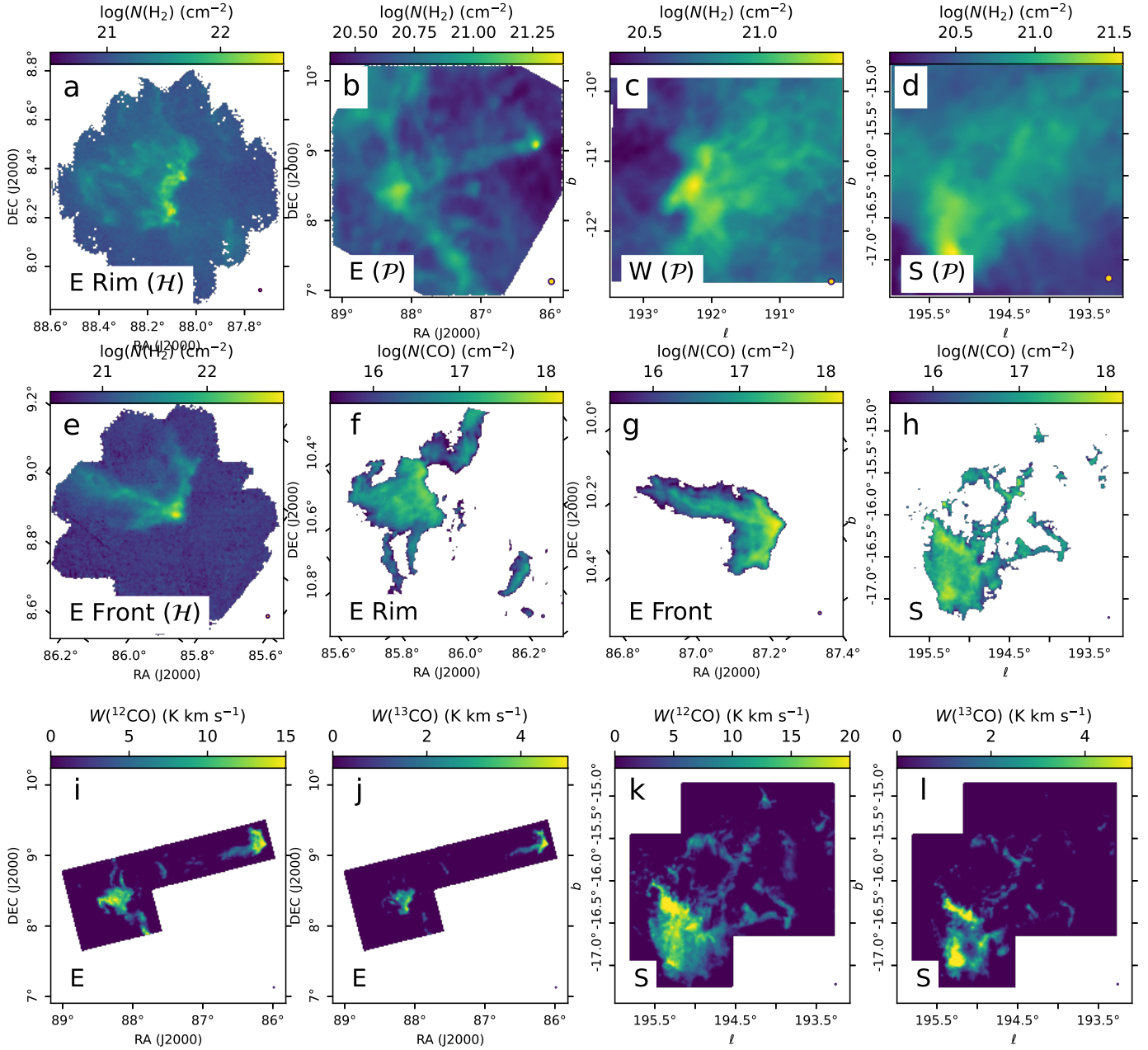
**Table F.1.** Values for the dendrogram regions.

(a) Field (ISO)	(b)	(c) $\Sigma T_{\text{mb}}$ [ $10^4$ K]	(d) $A$ [ $10^3$ arcmin $^2$ ]	(e) $v_{\text{cen}}$ [km s $^{-1}$ ]	(f) $\sigma_v$ [km s $^{-1}$ ]	(g) $M$ [M $_\odot$ ]	(h) $dM$ [M $_\odot$ ]	(i) $\alpha_{\text{vir}}$	(j) $d\alpha_{\text{vir}}$
E (12CO)	Rim	5.5 ± 13.4	98.9 ± 201.7	11.1 ± 1.8	0.5 ± 0.2	55.4 ± 135.9	21.5 ± 52.7	12.9 ± 12.3	2.7 ± 2.6
	Front	5.9 ± 9.9	95.8 ± 150.8	12.1 ± 0.2	0.3 ± 0.1	60.1 ± 100.0	23.3 ± 38.8	2.8 ± 1.7	0.6 ± 0.4
	Center	0.4 ± 0.7	18.4 ± 21.8	12.4 ± 1.6	0.3 ± 0.1	4.0 ± 7.0	1.6 ± 2.7	18.4 ± 17.0	3.9 ± 3.6
	Noise	0.0 ± 0.0	3.1 ± 0.0	12.4 ± 0.0	0.3 ± 0.0	0.5 ± 0.0	0.2 ± 0.0	23.4 ± 0.0	5.0 ± 0.0
	Body	69.0 ± 99.8	1169.7 ± 1717.1	10.0 ± 0.6	0.4 ± 0.2	908.3 ± 1313.5	352.5 ± 509.8	4.4 ± 7.9	0.9 ± 1.7
W (12CO)	Front leg	2.7 ± 3.0	71.2 ± 76.0	8.9 ± 0.2	0.3 ± 0.1	36.1 ± 39.8	14.0 ± 15.4	2.5 ± 2.0	0.5 ± 0.4
	Back leg	2.2 ± 3.6	34.4 ± 49.0	13.3 ± 0.6	0.4 ± 0.2	28.3 ± 47.9	11.0 ± 18.6	7.7 ± 7.8	1.6 ± 1.7
	Wings	4.0 ± 7.3	117.0 ± 198.1	8.8 ± 1.6	0.4 ± 0.2	52.7 ± 95.5	20.5 ± 37.0	7.8 ± 8.9	1.6 ± 1.9
	Spine	1.6 ± 1.5	32.0 ± 28.7	9.9 ± 0.1	0.2 ± 0.1	20.4 ± 19.6	7.9 ± 7.6	1.6 ± 0.7	0.3 ± 0.1
	Head	3.3 ± 3.8	47.2 ± 52.4	10.3 ± 0.2	0.3 ± 0.1	43.2 ± 49.9	16.8 ± 19.4	1.4 ± 0.5	0.3 ± 0.1
S (12CO)	Blobs	0.2 ± 0.4	13.1 ± 14.0	8.4 ± 3.4	0.3 ± 0.1	3.0 ± 4.8	1.2 ± 1.9	19.4 ± 12.7	4.1 ± 2.7
	Body	94.7 ± 144.1	1252.8 ± 1893.4	-0.5 ± 1.6	0.8 ± 0.6	702.7 ± 1069.6	272.7 ± 415.1	19.4 ± 20.1	4.1 ± 4.3
	Head	33.7 ± 68.4	445.3 ± 829.3	-1.0 ± 1.4	0.7 ± 0.6	250.0 ± 507.9	97.0 ± 197.1	11.4 ± 6.8	2.4 ± 1.4
	Legs	2.5 ± 4.7	67.5 ± 115.6	0.1 ± 1.9	0.4 ± 0.2	18.4 ± 34.7	7.1 ± 13.5	11.2 ± 9.5	2.4 ± 2.0
	Cloud	1.2 ± 1.7	71.1 ± 92.9	9.5 ± 0.4	0.3 ± 0.1	8.6 ± 12.3	3.3 ± 4.8	10.8 ± 7.1	2.3 ± 1.5
E (13CO)	Noise	0.1 ± 0.2	10.0 ± 10.7	0.4 ± 2.3	0.4 ± 0.2	1.1 ± 1.5	0.4 ± 0.6	42.5 ± 27.1	9.0 ± 5.8
	Rim	1.7 ± 2.6	90.1 ± 133.4	10.8 ± 0.9	0.4 ± 0.2	21.3 ± 33.7	8.3 ± 13.1	21.2 ± 23.5	4.5 ± 5.0
	Front	1.9 ± 2.4	94.2 ± 120.8	11.9 ± 0.2	0.3 ± 0.1	24.2 ± 30.4	9.4 ± 11.8	7.0 ± 8.9	1.5 ± 1.9
	Center	0.1 ± 0.1	17.7 ± 13.2	10.5 ± 2.2	0.2 ± 0.0	1.6 ± 1.3	0.6 ± 0.5	10.6 ± 5.9	2.3 ± 1.3
	Noise	0.5 ± 0.0	0.7 ± 0.0	-28.8 ± 0.0	0.6 ± 0.0	6.1 ± 0.0	2.4 ± 0.0	4.1 ± 0.0	0.9 ± 0.0
W (13CO)	Body	6.6 ± 10.6	361.8 ± 591.9	10.1 ± 0.8	0.3 ± 0.1	168.7 ± 271.0	65.5 ± 105.2	4.8 ± 6.2	1.0 ± 1.3
	Front leg	6.6 ± 10.6	361.8 ± 591.9	10.1 ± 0.8	0.3 ± 0.1	168.7 ± 271.0	65.5 ± 105.2	4.8 ± 6.2	1.0 ± 1.3
	Back leg	6.6 ± 10.6	361.8 ± 591.9	10.1 ± 0.8	0.3 ± 0.1	168.7 ± 271.0	65.5 ± 105.2	4.8 ± 6.2	1.0 ± 1.3
	Wings	0.1 ± 0.1	19.3 ± 16.1	9.3 ± 0.7	0.2 ± 0.1	2.2 ± 2.3	0.9 ± 0.9	11.7 ± 5.4	2.5 ± 1.1
	Spine	0.7 ± 0.8	44.6 ± 43.8	9.6 ± 0.1	0.2 ± 0.0	18.9 ± 20.2	7.4 ± 7.8	1.1 ± 0.6	0.2 ± 0.1
S (13CO)	Blobs	0.0 ± 0.0	7.2 ± 5.7	10.1 ± 2.4	0.2 ± 0.1	1.0 ± 1.0	0.4 ± 0.4	14.9 ± 10.2	3.2 ± 2.2
	Body	3.8 ± 12.4	192.6 ± 607.7	-0.8 ± 1.4	0.4 ± 0.3	65.2 ± 213.8	25.3 ± 83.0	32.9 ± 17.4	7.0 ± 3.7
	Head	6.6 ± 12.3	312.9 ± 571.4	-1.3 ± 1.5	0.5 ± 0.4	113.0 ± 211.5	43.9 ± 82.1	11.6 ± 10.0	2.5 ± 2.1
	Legs	0.3 ± 0.4	32.1 ± 44.3	-0.2 ± 1.6	0.3 ± 0.1	4.8 ± 7.7	1.9 ± 3.0	14.3 ± 15.5	3.0 ± 3.3

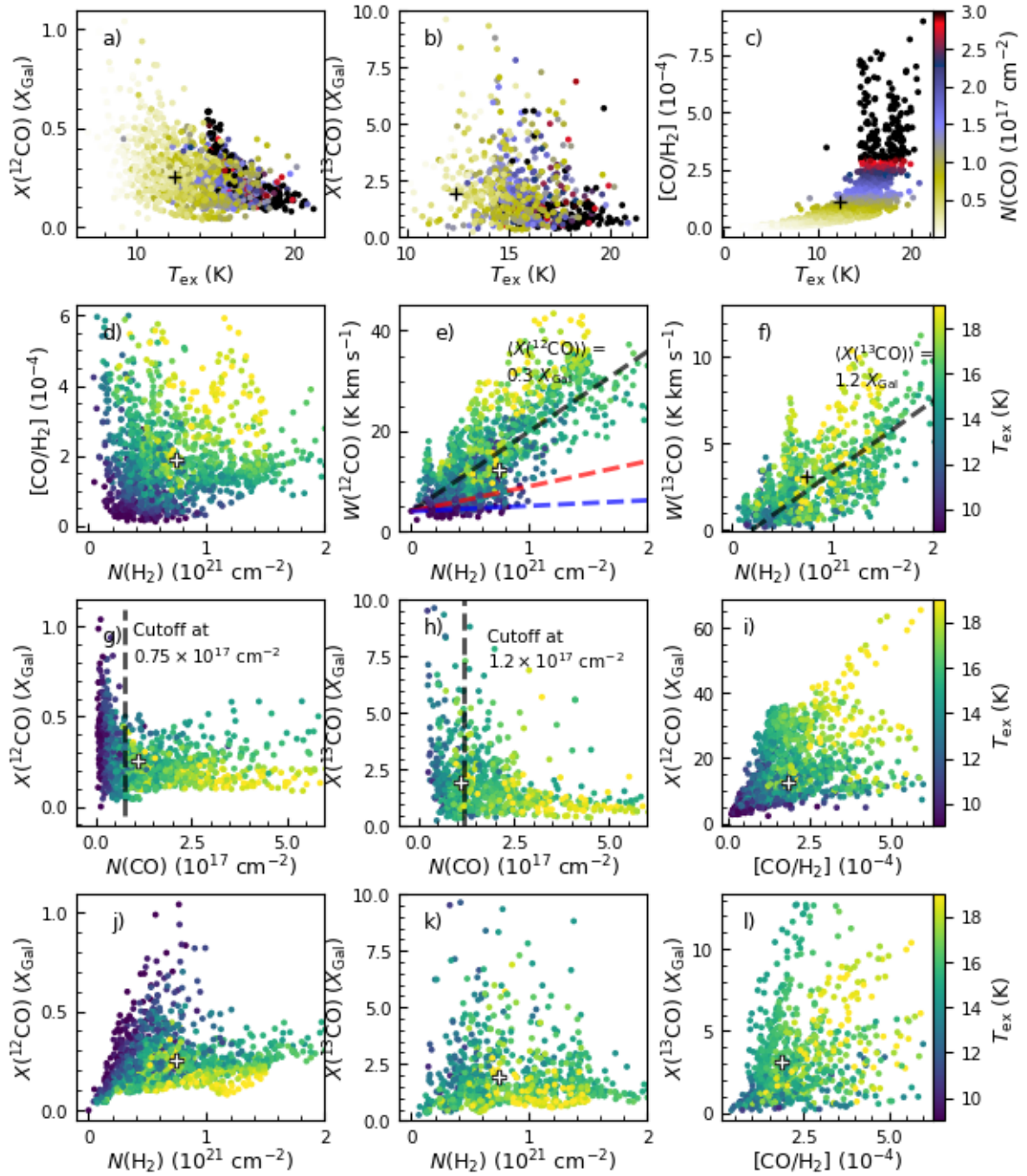
**Notes.** The columns are (a,b) Field and subregion; (c) sum of all the pixels in the subregion; (d) area in arcminutes; (e) central velocity; (f) velocity dispersion; (g,h) mass and uncertainty in mass of the structure; (i,j) virial alpha and uncertainty of the structure. The values presented are the mean of the values for all dendrogram structures in the subregion, uncertainties are the 95th percentile minus mean value and the mean minus the 5th percentile value.



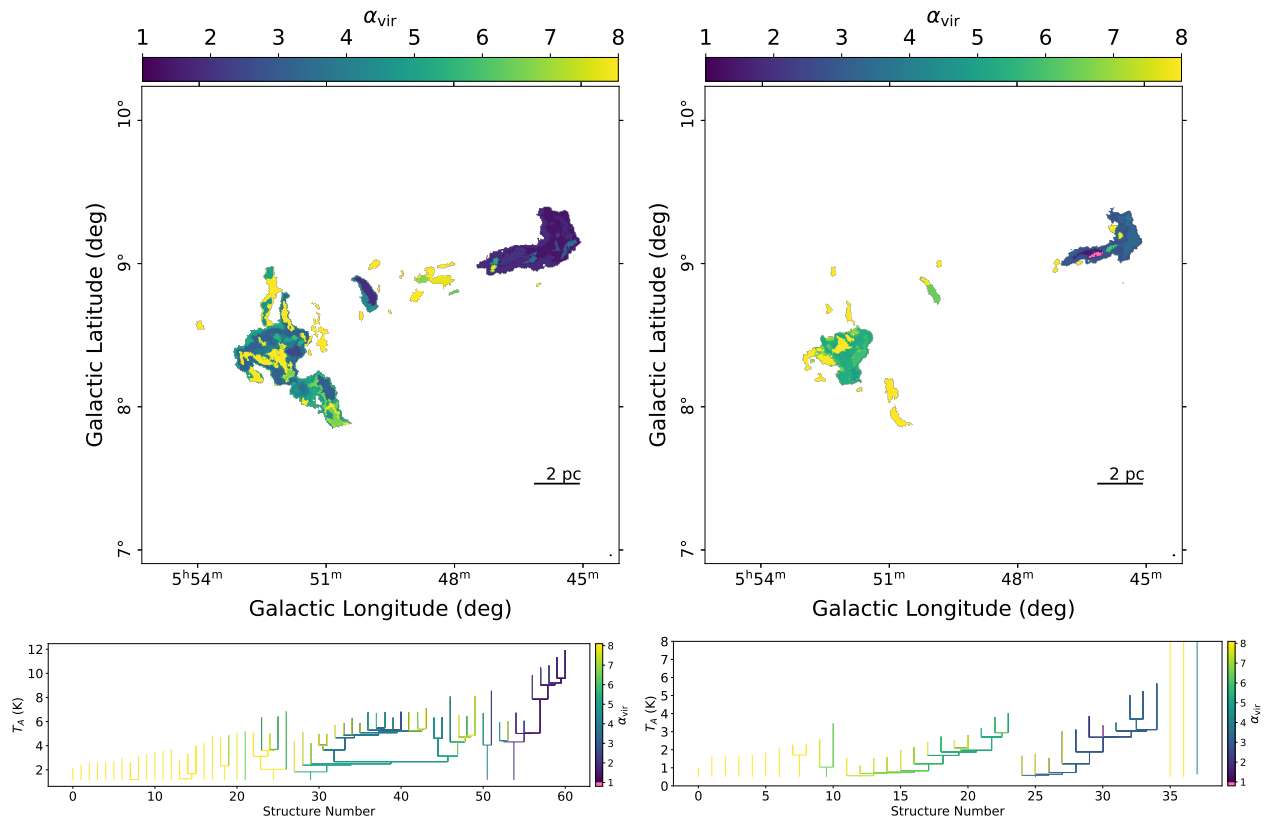
**Fig. C.3.** Same as Fig. C.1 for S. Meissa is located approximately above this image.



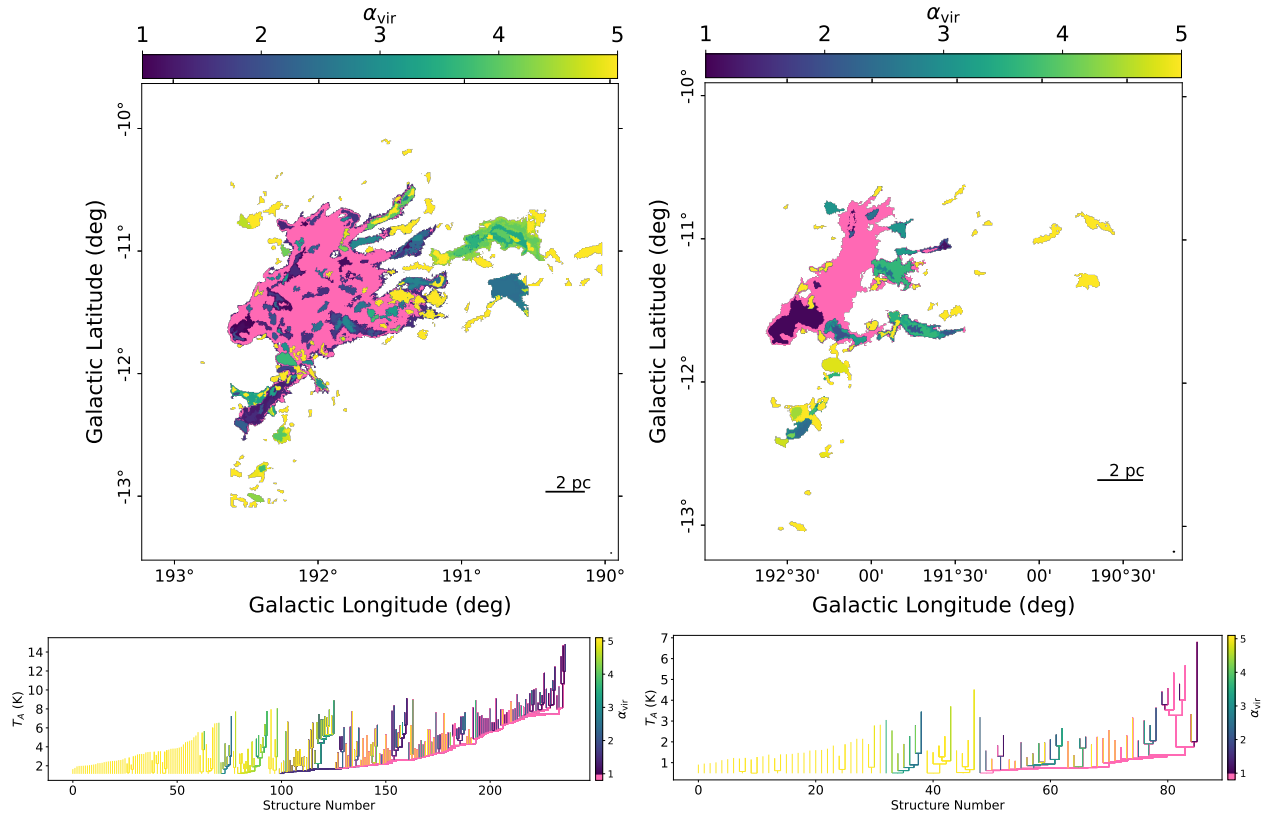
**Fig. D.1.** Column densities of the fields. (a,e)  $N(\text{H}_2)$  using *Herschel* SPIRE 250-500  $\mu\text{m}$  maps. (b-d)  $N(\text{H}_2)$  using *Planck*  $\tau_{353\text{GHz}}$  maps. (f-h)  $N(\text{CO})$  at the TRAO resolution. The  $N(\text{CO})$  map for E has been divided into the Rim (including the Center) and Front regions. (i-l) Integrated intensity  $W(\text{CO})$  of the E and S fields in  $^{12}\text{CO}$  (frames i, k) and  $^{13}\text{CO}$  (frames j, l). The name of the field is shown in the lower left corner, the beam in the lower right.



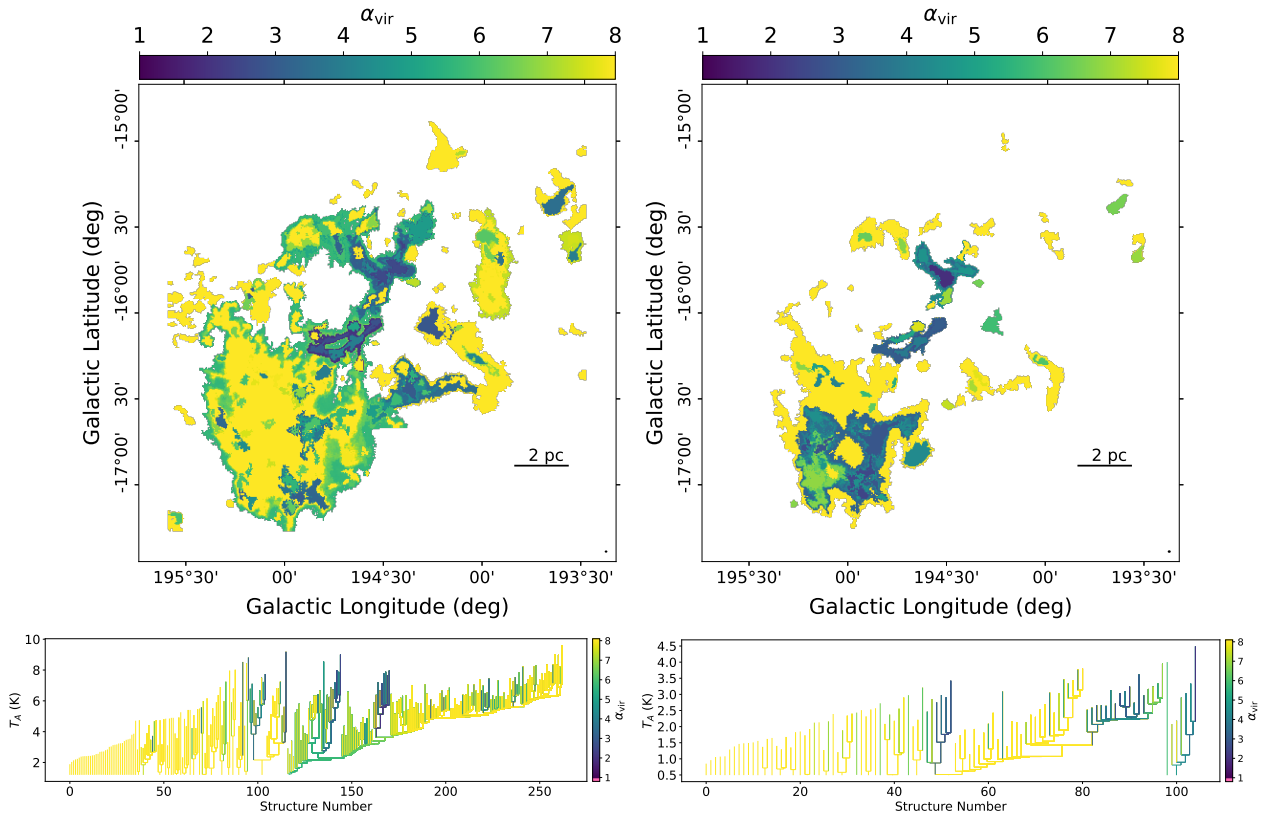
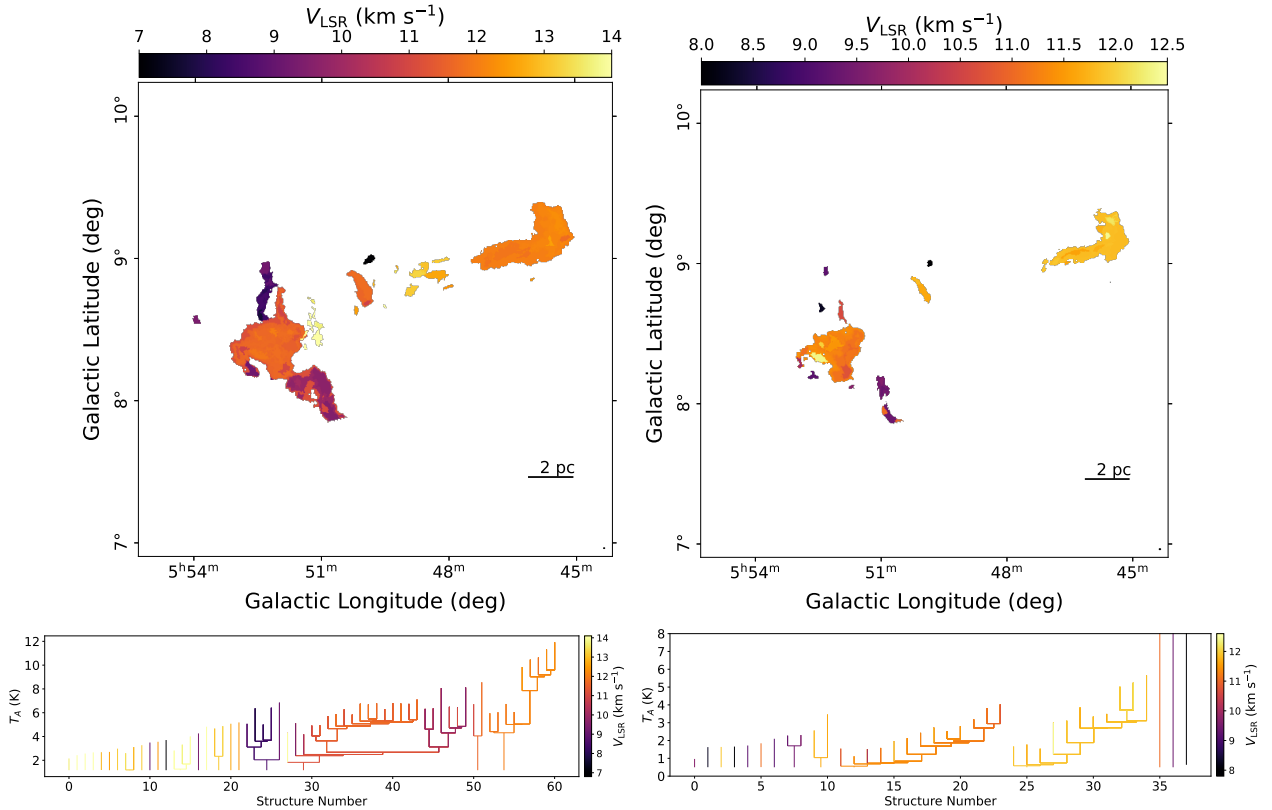
**Fig. E.1.** As Fig. 4.7 at the *Planck* resolution for the  $\lambda$  Orionis S region.

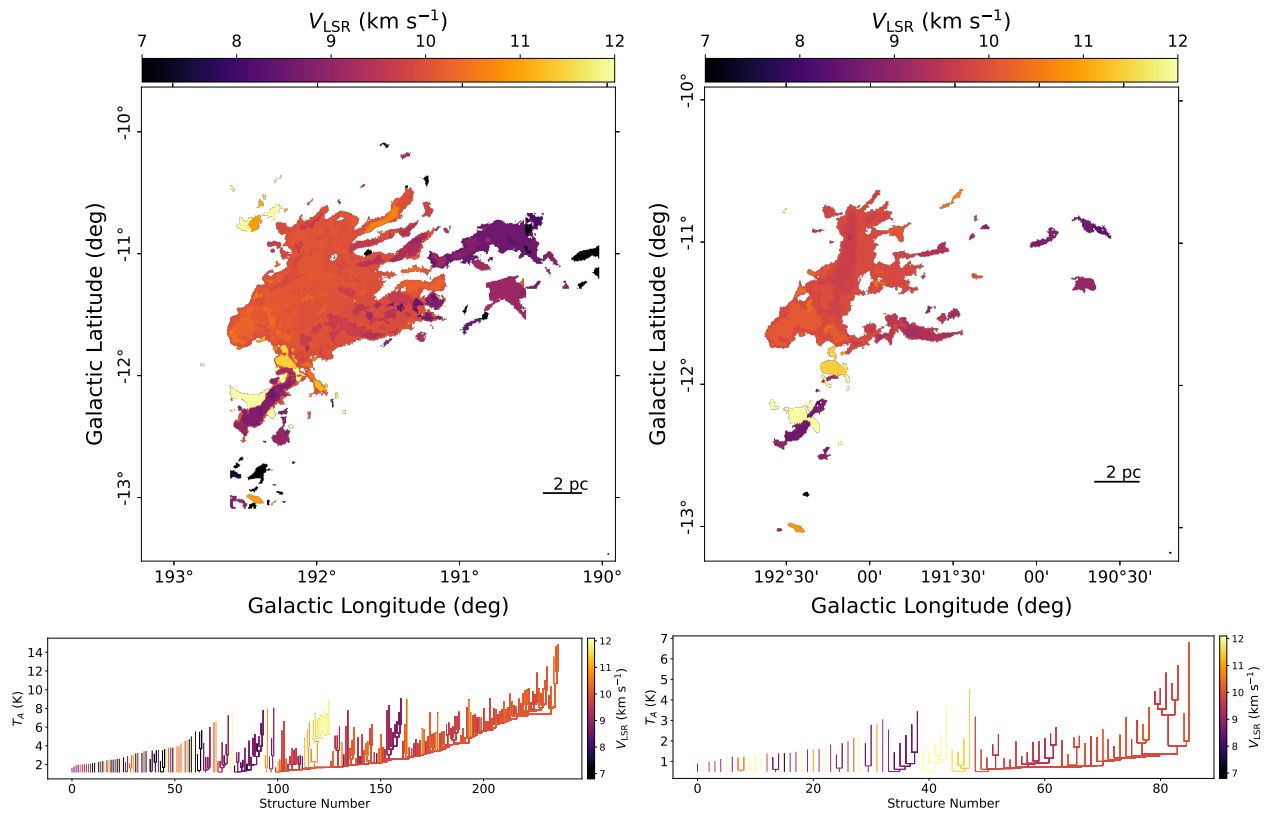
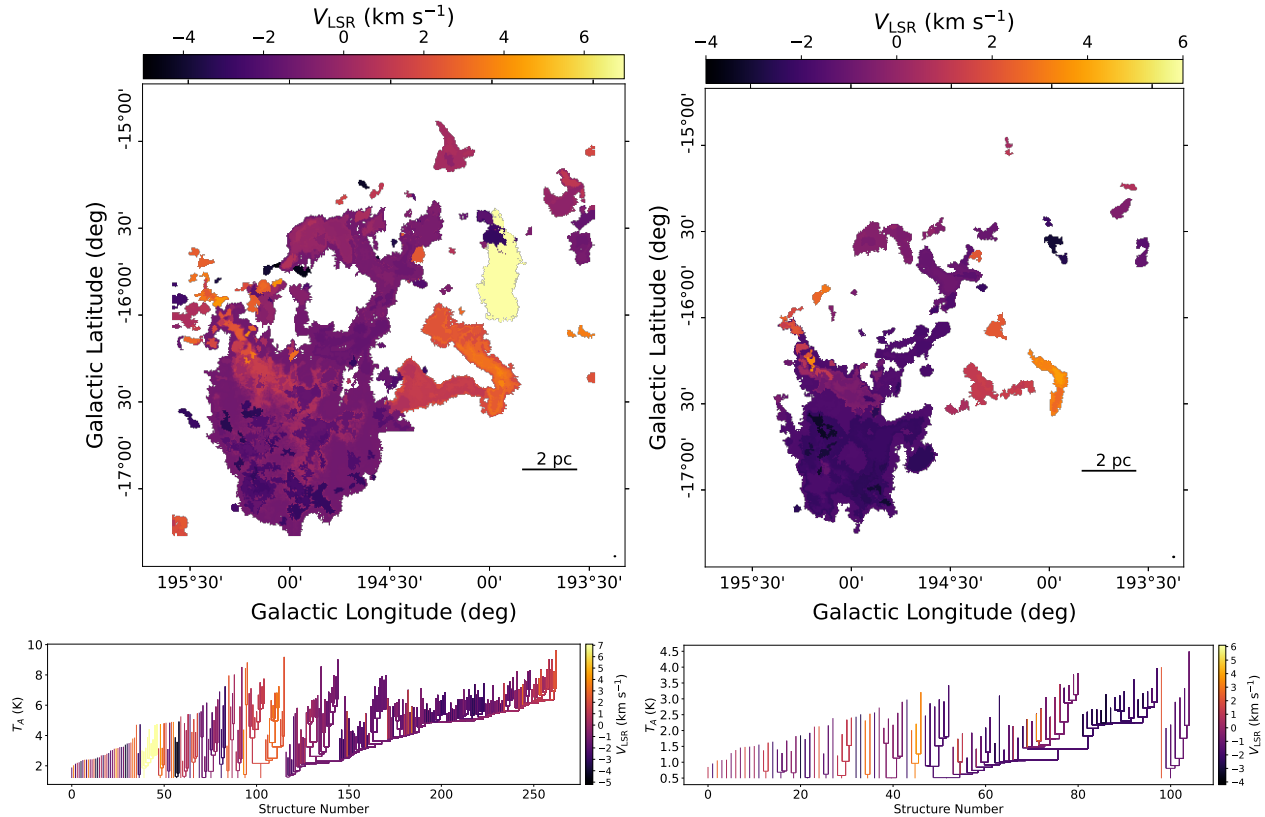


**Fig. F.1.** Virial alpha for E. Left column:  $^{12}\text{CO}$ , right column:  $^{13}\text{CO}$ . (Top): Map of  $\alpha_{\text{vir}}$ , plotting each substructure. (Bottom): Dendrogram tree of the cloud. Pink denotes structures with  $\alpha_{\text{vir}} \leq 1$ .



**Fig. F.2.** Same as Fig F.1 for W.

**Fig. F.3.** Same as Fig.F.1 for S.**Fig. F.4.** Central velocity of each substructure in E. Left column:  $^{12}\text{CO}$ , right column:  $^{13}\text{CO}$ . (Top): Map of  $v_{\text{cen}}$ . (Bottom): Dendrogram tree of the cloud.

**Fig. F.5.** Same as Fig. F.4 for W.**Fig. F.6.** Same as Fig. F.4 for S.